Available online at www.sciencedirect.com
SCIENCE DIRECT®
Journal of Computational Physics 207 (2005) 695–735
JOURNAL OF COMPUTATIONAL PHYSICS
www.elsevier.com/locate/jcp

A multipole-accelerated algorithm for close interaction of slightly deformable drops

Alexander Z. Zinchenko *, Robert H. Davis

Engineering Center, Department of Chemical and Biological Engineering, University of Colorado, ECCH 111, Campus Box, Boulder, CO 80309-0424, USA

Received 5 April 2004; received in revised form 11 January 2005; accepted 29 January 2005
Available online 17 March 2005

Abstract

An efficient multipole-accelerated boundary-integral algorithm is developed to study close-contact, three-dimensional interaction of two drops at zero Reynolds numbers and very small, but non-zero, capillary numbers Ca, when the drops are nearly spherical. The numerical difficulties (compared to the case of larger deformations) include severe stability limitations on the time step and a singular perturbation for $Ca \ll 1$, requiring very high surface resolution both in the small gap and in the "outer" region. The mesh triangle vertices are grouped into a large number of non-overlapping "patches," with economical, rotation-based multipole reexpansions to handle patch-to-patch interactions and limit the use of expensive direct summations. A novel concept of a "dynamical projective mesh" is developed, to maintain fixed-topology, gap-adaptive surface triangulations. For $O(10^5)$ boundary elements per drop in close contact, the algorithm has, at least, an order-of-magnitude advantage over the standard boundary-integral method, making such dynamical calculations feasible. In gravity-induced and shear-induced motion, exact results are obtained for the dynamics of the surface clearance h_{min} (which attains values less than 0.001 of the drop radii) and for the "separation angle" β_{sep} (determining the configuration when two drops in apparent contact start to separate). The shear flow problem is studied in the wide range of drop-to-medium viscosity ratios $0.25 \leqslant \lambda \leqslant 10$. Comparisons are made with prior and extended asymptotic theories of coalescence (based on matching the thin-film solution with the outer solution for spherical drops) to determine their range of validity and assess the "pumping flow" effect neglected in the theories. Pumping flow is most important for small λ and/or nearly head-on collisions; otherwise, the drops move past each other with too little time for the pumping flow to have a strong effect. The asymptotic techniques are extended to $\lambda \gg 1$, and shown to be very accurate for $\lambda = 4$ and 10 in the wide range of $Ca \ll 1$. Scaling laws for h_{min} and β_{sep} are found, both numerically and analytically; in particular, for $\lambda = O(1)$, β_{sep} approaches its limiting

* Corresponding author. Tel.: +1 303 492 0475/7471; fax: +1 303 492 4341.
E-mail addresses: zinchenk@spot.colorado.edu (A.Z. Zinchenko), robert.davis@colorado.edu (R.H. Davis).

0021-9991/$ - see front matter
doi:10.1016/j.jcp.2005.01.026

value $\pi/2$ (corresponding to zero "driving force" in the asymptotic theory) extremely slowly, with a difference of $O(Ca^{1/3})$, as $Ca \to 0$.

Keywords: Multipole methods; Deformable drops; Hydrodynamical interaction; Coalescence; Stokes flow

1. Introduction

Low Reynolds number motion of interacting drops is a fundamental problem relevant to emulsion sedimentation and rheology, and to drop coalescence and breakup. For zero capillary numbers, $Ca = 0$ (Ca being the ratio of viscous and surface tension forces), when the drops remain spherical, numerous semi-analytical studies have investigated hydrodynamical interactions, collision efficiencies, and rheological and sedimentational properties of semi-dilute and moderately concentrated emulsions. For moderate and large deformations, $Ca = O(1)$, more recent numerical work revealed a number of qualitatively new features, including deformation effects on self-diffusion [1], interaction-induced capture, cusping and breakup [2–5], non-Newtonian emulsion rheology [6–8], and a Koch–Shaqfeh [9] type of instability in very large systems of sedimenting drops [10,11]. For moderate deformations, the boundary-integral approach pioneered by Rallison and Acrivos [12] is the most appropriate tool (at Reynolds number $Re = 0$); when combined with multipole acceleration techniques [8,10], it has even allowed long-time simulations of as many as 1200 drops [11]. Somewhat ironically, these methods, so successful for large deformations, start to stall as the deformation is reduced, and they become completely prohibitive for interacting drops at $Ca \to 0$. One reason is a very tight stability limitation on the time step stemming from the Courant condition. Another difficulty is localization of stress requiring very high resolution in the narrow gap between two drops in close approach; less obvious, the outer region (away from the gap) also needs unlimited resolution as $Ca \to 0$. For a straightforward boundary-integral method with non-adaptive meshes, the CPU time required for a typical two-drop interaction would scale severely, faster than $Ca^{-3.5}$, thus totally prohibiting convergent calculations at $Ca \to 0$. On the other hand, $Ca \ll 1$ interactions, although they do not seem to offer as many qualitative features as large-deformation interactions do (in particular, breakup is excluded), have been of great practical interest (e.g. [13–15]), because they represent the most typical situation for emulsion drops with $Re \ll 1$, and they are most relevant to drop coalescence. The condition $Ca \ll 1$ does not generally warrant the neglect of deformation, since it acts as a singular perturbation precluding drops from touching, unless attractive molecular forces come into play [16,17]. In contrast, spherical drops make contact in a finite time [18–20], even without molecular attractions. Accordingly, there is a strong effect of small deformations on coalescence in many cases; drops with moderate or large deformations typically do not reach separations small enough for van der Waals forces to become significant.

Asymptotic thin-film solutions, instead of prohibitive full numerical solutions, have been used for some time (e.g. [16,17,21]) to describe head-on collisions of two slightly deformable drops. Recently, the asymptotic approach has been extended to glancing collisons [22] by matching the axisymmetrical, local thin-film solution in the gap with the outer solution for two spherical drops in a 3D motion. The outer solution provides the time-dependent "contact" force, which serves as a lubrication force to close the local, integro-differential thin-film equations in the gap. The approximation of local axial symmetry of the film (which follows from the asymptotic analysis [22]) greatly simplifies the solution. The initial conditions for the thin film are found by matching with the outer trajectory for spherical drops approaching contact, and the thin-film equations (which are numerically very stiff) for fully mobile surfaces are then solved by a new and efficient, absolutely stable algorithm. This technique has been applied to study many thousand trajectories and find thereby the coalescence efficiency (from the critical offsets for coalescence) by trial-and-error, both for

gravity-induced [22] and flow-induced [23] motions. Recent works [24,25] reveal, however, that the actual behavior of film drainage may be quite different from the predictions of the leading-order asymptotic theory that the method [22] is based upon. The authors [24,25] showed numerically for finite deformations, and analytically for $Ca \ll 1$, that the configuration of two drops pressed together in a uniaxial compression (head-on collision) reaches a steady state with non-zero gap thickness, due to the "pumping flow" effect, instead of long-time film thinning. Additionally, there remains some doubt in the experimental literature if the axial symmetry of the film is a correct assumption for non-axisymmetric collisions.

Since the asymptotic technique [22] is a very productive approach to coalescence efficiency calculations, as opposed to (nearly) prohibitive boundary-integral simulations at $Ca \ll 1$, it is of great interest to study if it is indeed a correct method for non-axisymmetrical interactions and to find its range of validity; in particular, it is important to determine if (and when) the neglect [22,23] of the pumping flow is an accurate assumption. In [22], a limited comparison between the asymptotic and boundary-integral results for gravity-induced motion was made for matching viscosities ($\lambda = 1$), demonstrating an approximate agreement for a minimum surface clearance of $h_{\min} \approx 0.007 a_2$ (where a_2 is the larger of the two radii) to within a factor of 2; the capillary number in this test was not too small, and it was unclear if the asymptotic theory would become more accurate at $Ca \to 0$. Similar comparisons were made [23] for glancing collisions in a uniaxial compressional flow at $\lambda = 1$. A puzzling discrepancy between asymptotic and numerical results was observed in the separation zone, and it did not seem to change appreciably as the capillary number was reduced several-fold; limitations of the boundary-integral code at that time did not allow us to proceed further. Moreover, no attempts have been made at all to validate the asymptotic theory of coalesence [22] for arbitrary drop-to-medium viscosity ratios λ.

In the present work, we have developed a novel, and much more powerful algorithm to study three-dimensional $Ca \ll 1$ interaction of two surfactant-free drops in much greater detail. For simplicity, molecular attractions are neglected. Our goal is to obtain exact results at much smaller capillary numbers than before, and at arbitrary viscosity ratios λ, for comparisons with the asymptotic theories [22,23], and also to extend these theories to high λ. In Section 2, the boundary-integral formulation is outlined. An essential feature is multipole acceleration (Section 3.2), which is done in the spirit of our multidrop algorithms [8,10,11]. The difference is that, for many drops with finite deformations, multipole acceleration was designed to be efficient for moderate surface triangulations ($O(10^3)$ boundary elements per drop), while in the present problem, we seek an efficient method for only two drops but with very high surface resolutions (up to $O(10^5)$ elements per drop) relevant to $Ca \ll 1$ interactions in close contact, to make boundary-integral calculations much less prohibitive in this range. Accordingly, many steps in the present multipole acceleration scheme are different. A substantially new concept of a "dynamical projective mesh" is also developed (Section 3.3). Although specific for the current problem ($Ca \ll 1$ interactions), this method is found to be an efficient and relatively simple way to adapt fixed topology surface triangulations to the gap. It has a well-controlled mesh, no need for interpolations, and relatively soft stability constraints (Section 3.4). The asymptotic techniques are outlined in Section 4, and an extension is made to high viscosity ratios $\lambda \geqslant O(Ca^{-1/2})$, including a new, absolutely stable algorithm for the thin-film equations with partially mobile surfaces, and a new matching condition with the outer trajectory suitable for $\lambda \gg 1$; the original techniques [22] were designed to work only for $\lambda \ll Ca^{-1/2}$ (and $\lambda \gg |\ln Ca| Ca^{1/2}$). In Sections 5 and 6, on numerical results, we pay particular attention to numerical convergence of our boundary-integral calculations in the difficult range $Ca \ll 1$, since the main goal is to check the asymptotic theories with exact results. Detailed comparisons between the theories and simulations are made for the dynamics of the surface clearance $h_{\min}$ (which attains very small values, $\sim 10^{-4}$–10^{-3} of the drop radii), and for the separation angle (determining the configuration when the two drops in "apparent contact" start to separate). Both gravity-induced motion of unequal drops and shear-induced motion of two equal drops are considered; the second problem is studied in greater detail, including a wide range of capillary numbers $Ca \geqslant 0.005$ and viscosity ratios $0.25 \leqslant \lambda \leqslant 10$. These comparisons greatly clarify the range of validity of the asymptotic

method, which substantially depends on λ. The scaling laws for $h_{\min}$ and the separation angle at $Ca \to 0$ are also found.

Multipole acceleration, the biggest part of our code, could be possibly done in a different manner using the hydrodynamical version of FMM developed in a general form by Sangani and Mo [26]. Their method relies on hierarchy of space decompositions by Cartesian grids and the use of low-order multipoles. In contrast, our method features a broad use of rotation-based schemes and "economical truncation" of high-order multipole expansions (and not using hierarchy of space decompositions). Unfortunately, within the scope of the present work, it was not possible to compare the efficiency of the two, vastly different techniques.

All timings below are for a single-processor AMD PC, with Athlon XP 2600 + CPU.

2. Boundary-integral formulation

Consider two deformable drops of density ρ' and viscosity μ' moving in an unbounded quiescent liquid of density ρ_e and viscosity μ_e under creeping flow ($Re = 0$) conditions. The gravity acceleration is $\boldsymbol{g}$, and $\boldsymbol{u}_\infty(\boldsymbol{x})$ is the unperturbed flow velocity away from the drops. The standard boundary-integral equation [12] for the interfacial velocity $\boldsymbol{u}(\boldsymbol{y})$ to be solved at each time step takes the form

$$\boldsymbol{u}(\boldsymbol{y}) = 2\kappa \sum_{\beta=1}^{2} \int_{S_\beta} \boldsymbol{u}(\boldsymbol{x}) \cdot \boldsymbol{T}(\boldsymbol{x}-\boldsymbol{y}) \cdot \boldsymbol{n}(\boldsymbol{x})\, \mathrm{d}S_x + \boldsymbol{F}(\boldsymbol{y}), \tag{2.1}$$

where $\kappa = (\lambda - 1)/(\lambda + 1)$, $\lambda = \mu'/\mu_e$ is the viscosity ratio, S_β ($\beta = 1, 2$) is a drop surface,

$$\boldsymbol{T}(\boldsymbol{r}) = \frac{3}{4\pi} \frac{\boldsymbol{rrr}}{r^5} \tag{2.2}$$

is the stresslet corresponding to the free-space Green tensor (with unit viscosity)

$$\boldsymbol{G}(\boldsymbol{r}) = -\frac{1}{8\pi}\left[\frac{\boldsymbol{I}}{r} + \frac{\boldsymbol{rr}}{r^3}\right], \tag{2.3}$$

and $\boldsymbol{n}(\boldsymbol{x})$ is the outward unit normal at $\boldsymbol{x} \in S_\beta$. The inhomogeneous term is

$$\boldsymbol{F}(\boldsymbol{y}) = \frac{2\boldsymbol{u}_\infty(\boldsymbol{y})}{1+\lambda} + \frac{2}{\mu_e(1+\lambda)} \sum_{\beta=1}^{2} \int_{S_\beta} f(\boldsymbol{x}) \boldsymbol{n}(\boldsymbol{x}) \cdot \boldsymbol{G}(\boldsymbol{x}-\boldsymbol{y})\, \mathrm{d}S_x, \tag{2.4}$$

where

$$f(\boldsymbol{x}) = 2\sigma k(\boldsymbol{x}) + (\rho_e - \rho')gz - \langle 2\sigma k(\boldsymbol{x}) + (\rho_e - \rho')gz \rangle_\beta, \tag{2.5}$$

where σ is the constant surface tension, $k(\boldsymbol{x}) = \frac{1}{2}(k_1 + k_2)$ is the mean surface curvature at $\boldsymbol{x}$, and z is the Cartesian coordinate in the direction of gravity. By $\langle \cdots \rangle_\beta$, we denote the surface average over S_β; the essence of considering the fluctuations from $\langle \cdots \rangle_\beta$ in (2.5) without affecting the value of the integral (2.4) is to minimize the variation of $f(\boldsymbol{x})$ over S_β, thereby increasing the efficiency of multipole acceleration (Section 3).

To reduce the number of iterations in solving (2.1) for extreme viscosity ratios $\lambda \ll 1$ or $\lambda \gg 1$, this system is subject to Wielandt's deflation [27,28] and reformulated in terms of $\boldsymbol{w} = \boldsymbol{u} - \kappa \boldsymbol{u}'$, where the prime denotes the "rigid-body projection" of $\boldsymbol{u}$ (a convenient recipe for calculating $\boldsymbol{u}'$ is given by (11)–(15) of [29]). Introducing the fluctuations

$$\boldsymbol{Q}(\boldsymbol{x})|_{S_\beta} = \boldsymbol{w}(\boldsymbol{x}) - \langle \boldsymbol{w} \rangle_\beta, \tag{2.6}$$

the deflated system of equations takes the form

$$\boldsymbol{w}(\boldsymbol{y})|_{S_\alpha} = \kappa\left[2\sum_{\beta=1}^{2}\int_{S_\beta}\boldsymbol{Q}(\boldsymbol{x})\cdot\boldsymbol{T}(\boldsymbol{x}-\boldsymbol{y})\cdot\boldsymbol{n}(\boldsymbol{x})\,\mathrm{d}S_x + \langle\boldsymbol{w}\rangle_\alpha - \boldsymbol{w}'(\boldsymbol{y}) + \frac{\boldsymbol{n}(\boldsymbol{y})}{S_\alpha}\int_{S_\alpha}\boldsymbol{w}\cdot\boldsymbol{n}\,\mathrm{d}S\right] + \boldsymbol{F}(\boldsymbol{y}). \tag{2.7}$$

Once $\boldsymbol{w}$ is found, the interfacial velocity $\boldsymbol{u} = \boldsymbol{w} + \kappa\boldsymbol{w}'/(1-\kappa)$ can be recovered.

Two particular cases are of interest in the present work. One is a gravity-induced motion of two unequal drops in a quiescent liquid ($u_\infty = \mathbf{0}$). Characteristic length and velocity scales to make Eqs. (2.1)–(2.7) non-dimensional are chosen to be a_2 and $|\Delta\rho|ga_2^2/\mu_e$, respectively, where a_2 is the largest of the two non-deformed radii a_1, a_2, and $\Delta\rho = \rho' - \rho_e$. For consistency with earlier work [22,29], the capillary number is defined as

$$Ca = \frac{\mu_e\left|\boldsymbol{V}_1^\infty - \boldsymbol{V}_2^\infty\right|}{\sigma}, \quad \boldsymbol{V}_i^\infty = \frac{2}{9}\frac{(\lambda+1)}{\left(\lambda+\frac{2}{3}\right)}\frac{a_i^2\Delta\rho\boldsymbol{g}}{\mu_e} \tag{2.8}$$

with $\boldsymbol{V}_i^\infty$ being the settling velocities of isolated spherical drops. The second case is a relative motion of two freely suspended drops ($\Delta\rho = 0$) in a steady shear $\boldsymbol{u}_\infty(\boldsymbol{x}) = (-\gamma x_2, 0, 0)$. The length and velocity scales to non-dimensionalize (2.1)–(2.7) are $2R$ and $2\gamma R$, where $R = a_1a_2/(a_1+a_2)$ is the reduced radius; the capillary number is

$$Ca = 2\mu_e\gamma R/\sigma. \tag{2.9}$$

3. Numerical method

3.1. Discretization

Drop surfaces are discretized by unstructured meshes with a fixed topology. For any smooth function $\varphi(\boldsymbol{x})$ on S_α, a second-order approximation is used

$$\int_{S_\alpha}\varphi(\boldsymbol{x})\,\mathrm{d}S \approx \sum_{\boldsymbol{x}_j\in S_\alpha}\varphi(\boldsymbol{x}_j)\Delta S_j, \tag{3.1}$$

where the summation is over all mesh triangle vertices $\boldsymbol{x}_j$ (called collocation nodes) on S_α, and ΔS_j is the "surface area associated with node $\boldsymbol{x}_j$." Unlike in our previous boundary-integral work [4,8,10,11,29], where ΔS_j was simply one-third of the sum of flat triangle areas sharing node $\boldsymbol{x}_j$ (following [30]), here ΔS_j is constructed very differently, based on the new idea of a "projective mesh," to allow for adaptivity in near-contact areas; projective meshes are also used for a new, non-iterative calculation of normals and curvatures in nodes $\boldsymbol{x}_j$ (see Section 3.3 for more detail). Boundary integrals (2.4) and (2.7) are subject to standard singularity subtractions (when $\boldsymbol{y}$ is on the integration surface) to make integrands O(1), as $\boldsymbol{x}\to\boldsymbol{y}$. Near-singularity subtractions (when $\boldsymbol{y}$ is close to another surface) in the form [10] are also used to considerably reduce numerical errors for drops in close approach (although they do not completely eliminate the unbounded behavior of the double-layer integrands (2.7)). Accordingly, integrals (2.4) and (2.7) are approximated as

$$\int_{S_\beta} f(\boldsymbol{x})\boldsymbol{n}(\boldsymbol{x})\cdot\boldsymbol{G}(\boldsymbol{x}-\boldsymbol{y})\,\mathrm{d}S_x = \sum_{\boldsymbol{x}_j\in S_\beta} f(\boldsymbol{x}_j)\boldsymbol{G}(\boldsymbol{x}_j-\boldsymbol{y})\cdot\boldsymbol{n}(\boldsymbol{x}_j)\Delta S_j - \Theta(\boldsymbol{y},\beta)f(\boldsymbol{x}^*)\sum_{\boldsymbol{x}_j\in S_\beta}\boldsymbol{G}(\boldsymbol{x}_j-\boldsymbol{y})\cdot\boldsymbol{n}(\boldsymbol{x}_j)\Delta S_j, \tag{3.2}$$

and

$$\int_{S_\beta} \boldsymbol{Q}(\boldsymbol{x}) \cdot \boldsymbol{T}(\boldsymbol{x}-\boldsymbol{y}) \cdot \boldsymbol{n}(\boldsymbol{x})\, \mathrm{d}S_x \approx \sum_{\boldsymbol{x}_j \in S_\beta} \boldsymbol{Q}(\boldsymbol{x}_j) \cdot \boldsymbol{T}(\boldsymbol{x}_j-\boldsymbol{y}) \cdot \boldsymbol{n}(\boldsymbol{x}_j) \Delta S_j - \Theta(\boldsymbol{y},\beta)\boldsymbol{Q}(\boldsymbol{x}^*) \cdot \sum_{\boldsymbol{x}_j \in S_\beta} \boldsymbol{T}(\boldsymbol{x}_j-\boldsymbol{y}) \cdot \boldsymbol{n}(\boldsymbol{x}_j) \Delta S_j + \begin{cases} \frac{1}{2}\boldsymbol{Q}(\boldsymbol{y}), & \boldsymbol{y} \in S_\beta \\ 0 & \boldsymbol{y} \notin S_\beta. \end{cases} \tag{3.3}$$

Here, $\boldsymbol{x}^*$ is the collocation node on S_β that is closest to $\boldsymbol{y}$ (Fig. 1)

$$\Theta(\boldsymbol{y},\beta) = \max\left\{1 - \frac{\|\boldsymbol{y}-\boldsymbol{x}^*\|^2}{h_o^2}, 0\right\}, \tag{3.4}$$

and h_o is the threshold parameter (set to 0.25 a_β in the present work, where a_β is the non-deformed drop radius). For $\boldsymbol{y} \in S_\beta$, (3.2) and (3.3) are just standard singularity subtractions (with $\boldsymbol{x}^* = \boldsymbol{y}$, $\Theta = 1$, and node $\boldsymbol{x}_j = \boldsymbol{y}$ excluded from the summations). According to (3.4), near-singularity subtractions ($\boldsymbol{y} \in S_\alpha \neq S_\beta$) are in effect only when $\boldsymbol{y}$ is close to another surface ($\|\boldsymbol{y}-\boldsymbol{x}^*\| < h_o$). For $\|\boldsymbol{y}-\boldsymbol{x}^*\| \ll h_o$, Θ is close to 1, and the subtracted terms (the second sums in (3.2) and (3.3)) effectively cancel near-singular behavior of the first sums in these equations; at the same time, the subtracted terms disappear in the limit of fine triangulations. Gradual transition of Θ to zero, as $\|\boldsymbol{y}-\boldsymbol{x}^*\| \to h_o$, serves the smoothness of the near-singularity subtractions. Relations (3.2) and (3.3) differ from the original near-singularity subtractions of Loewenberg and Hinch [6] by the presence of the threshold factor Θ, making multipole-based calculations of the subtracted terms (necessary only for $\Theta \neq 0$) more efficient without any appreciable loss of accuracy. For double-layer calculations, a different choice of the subtracted quantity $\boldsymbol{Q}^*$ (instead of $\boldsymbol{Q}(\boldsymbol{x}^*)$ in (3.3)) was suggested [8] based on the solution of a variational problem for $\boldsymbol{Q}^*$, to improve the spectral properties of the discretized double-layer operator. We have found that the variational approach loses advantage in the limit of very fine triangulations and so the simplest choice $\boldsymbol{Q}^* = \boldsymbol{Q}(\boldsymbol{x}^*)$ was used in the present work.

3.2. Fast calculation of boundary integrals

Direct point-to-point summations in (3.2) and (3.3) have $O(N_\triangle^2)$ cost per time step (where $N_\triangle$ is the number of triangular boundary elements per drop), and could not succeed in the present calculations, with $N_\triangle$ up to $O(10^5)$ and up to $O(10^4$–$10^5)$ time steps for a single run due to very tight stability limitations for $N_\triangle \gg 1$ and $Ca \ll 1$. A far more efficient, multipole-accelerated scheme for calculating boundary-integral operators (2.4) and (2.7) at large $N_\triangle$ is used, similar in the spirit to the multidrop codes [8,10,11]. Those codes, however, were designed to be efficient for large systems of drops ($N \sim 10^2$–10^3) with moderate resolutions $N_\triangle \sim 10^3$ and moderate deformations. Numerous new elements are needed in the present,

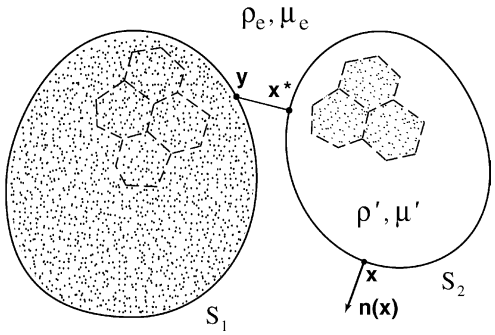

Fig. 1. Schematic for two deformable drops; the partition of mesh nodes into non-overlapping "patches" is also shown (not to scale).

two-drop high resolution problem to obtain a significant advantage over standard point-to-point summations. First, space decomposition of collocation nodes is done differently. Second, calculation of the subtracted terms (second sums in (3.2) and (3.3)) also requires multipole acceleration (while in our multidrop codes at $N_\triangle \sim 10^3$ these subtractions were relatively inexpensive and handled in a simple, point-to-point manner); accordingly, new issues arise regarding economical truncation bounds for multipole expansions/reexpansions associated with the subtracted terms in (3.2) and (3.3). All of these changes are detailed below.

First, we group collocation nodes $\boldsymbol{x}_j$ on each drop into a large number of non-overlapping sets called "patches" (Fig. 1). To generate patches, we choose some projection center $\boldsymbol{O}_\alpha (\alpha = 1, 2)$ inside drop S_α and use an auxiliary, crude, almost uniform unstructured mesh of $M_\triangle \gg 1$ triangles (with $M_\triangle/2 + 2$ vertices) inscribed into a unit sphere Ω centered at $\boldsymbol{O}_\alpha$. The methods to obtain such a mesh from regular polyhedra by a series of refinements are well known (e.g. [29,31]); in this manner, we obtain $M_\triangle = 20$, 60, 80, 180, 240, 320, etc. with maximum-to-minimum mesh edge ratio less than 1.19. Each collocation node $\boldsymbol{x}_j \in S_\alpha$ is then connected to $\boldsymbol{O}_\alpha$ to find the trace $\hat{\boldsymbol{x}}_j$ of $\boldsymbol{x}_j$ on the crude mesh polyhedron and the crude mesh node $\boldsymbol{z}_i$ on the unit sphere closest to $\hat{\boldsymbol{x}}_j$ (Fig. 2). This algorithm naturally partitions all $N_\triangle/2 + 2$ collocation nodes on S_α into $M_\triangle/2 + 2$ non-overlapping patches $\mathscr{B}_1, \mathscr{B}_2, \ldots$ associated with the vertices of the crude mesh; dual Voronoi polyhedron for the crude mesh (obtained by drawing bisecting planes to mesh edges) helps to further understand this construction. For drop surface triangulations adaptive to near-contact areas, it is advantageous to choose $\boldsymbol{O}_\alpha$ close to another surface (rather than at the drop center), thereby making the number of collocation nodes per patch closer to uniform; dynamical calculation of $\boldsymbol{O}_\alpha$ is discussed in Section 3.3. In the present work, we have found about 200–400 nodes per patch to be optimal for multipole acceleration in close approach. These patches are analogous to entire drops (or "blocks" of the drop size) in the multidrop codes [8,10,11].

For $\boldsymbol{y} = \boldsymbol{x}_i \in \mathscr{B}_\gamma$, contributions from $\boldsymbol{x}_j \in \mathscr{B}_\gamma$ $(\boldsymbol{x}_j \neq \boldsymbol{x}_i)$ to the RHS of (3.2) and (3.3) ("self-interactions") are handled in a pointwise manner, with joining pairs $(\boldsymbol{x}_i, \boldsymbol{x}_j)$ and $(\boldsymbol{x}_j, \boldsymbol{x}_i)$ in this operation for maximum efficiency. For the double-layer (3.3), these self-interactions are calculated on every iteration, as well as remaining operations in the first sum of (3.3). To unload iterations, however, operations in the second sum of (3.3) are greatly facilitated by precalculating the second-rank "subtraction tensor" $\boldsymbol{\Pi}$

$$\boldsymbol{\Pi}(\boldsymbol{y}, \beta) = \Theta(\boldsymbol{y}, \beta) \sum_{\boldsymbol{x}_j \in S_\beta} \boldsymbol{T}(\boldsymbol{x}_j - \boldsymbol{y}) \cdot \boldsymbol{n}(\boldsymbol{x}_j) \Delta S_j \ [\text{minus self} - \text{interaction contribution}], \tag{3.5}$$

which is independent of $\boldsymbol{Q}$.

The preiterative part of the algorithm (i.e., remaining operations in (3.2) and calculation of $\boldsymbol{\Pi}(\boldsymbol{y}, \beta)$, if $\lambda \neq 1$) now works as follows. A minimal spherical shell $\mathscr{D}_\gamma$ with center $\boldsymbol{x}^o_\gamma$ and radius d^o_γ is constructed

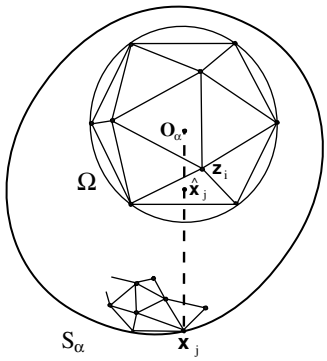

Fig. 2. The algorithm for mesh node partition into patches.

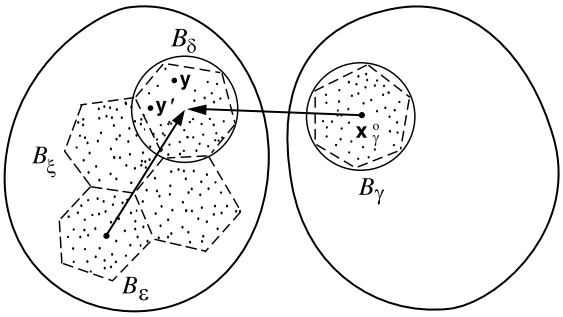

Fig. 3. Fast calculation of boundary-integrals. Contributions $\mathscr{B}_\gamma \to \boldsymbol{y}$, $\mathscr{B}_\varepsilon \to \boldsymbol{y}$ of patches $\mathscr{B}_\gamma$, $\mathscr{B}_\varepsilon$ ("well-separated" from $\mathscr{B}_\delta$) to boundary integrals for all $\boldsymbol{y} \in \mathscr{B}_\delta$ are calculated by cumulative reexpansions of Lamb's singular series. For $\boldsymbol{y}$ "well outside" $\mathscr{D}_\xi$, the $\mathscr{B}_\xi \to \boldsymbol{y}$ contribution is handled by pointwise calculation of Lamb's singular series. For $\boldsymbol{y}' \in \mathscr{B}_\delta$ (close to $\mathscr{B}_\xi$), the $\mathscr{B}_\xi \to \boldsymbol{y}'$ contribution is calculated by standard point-to-point summations.

around each patch $\mathscr{B}_\gamma$ (Fig. 3) with sufficient accuracy (following a simple stochastic procedure [10]). Note that our construction of patches seeks to minimize overlapping of spherical shells $\mathscr{D}_\gamma$ (Fig. 1), to increase the efficiency of multipole accelerations. The single-layer contributions of each patch $\mathscr{B}_\gamma$ to the sums (3.2) are expanded in Lamb's singular series

$$\sum_{\boldsymbol{x}_j \in \mathscr{B}_\gamma} f(\boldsymbol{x}_j)\boldsymbol{G}(\boldsymbol{x}_j - \boldsymbol{y}) \cdot \boldsymbol{n}(\boldsymbol{x}_j)\Delta S_j = \sum_{v=1}^{\infty} \left[\nabla \times (\boldsymbol{R}_\gamma \chi_{-(v+1)}) + \nabla \Phi_{-(v+1)} - \frac{(v-2)R_\gamma^2 \nabla p_{-(v+1)}}{2v(2v-1)} + \frac{(v+1)p_{-(v+1)}\boldsymbol{R}_\gamma}{v(2v-1)} \right] \tag{3.6}$$

and

$$\sum_{\boldsymbol{x}_j \in \mathscr{B}_\gamma} \boldsymbol{G}(\boldsymbol{x}_j - \boldsymbol{y}) \cdot \boldsymbol{n}(\boldsymbol{x}_j)\Delta S_j = \sum_{v=1}^{\infty} \left[\nabla \times (\boldsymbol{R}_\gamma \hat{\chi}_{-(v+1)}) + \nabla \hat{\Phi}_{-(v+1)} - \frac{(v-2)R_\gamma^2 \nabla \hat{p}_{-(v+1)}}{2v(2v-1)} + \frac{(v+1)\hat{p}_{-(v+1)}\boldsymbol{R}_\gamma}{v(2v-1)} \right], \tag{3.7}$$

where $\boldsymbol{R}_\gamma = \boldsymbol{y} - \boldsymbol{x}_\gamma^o$, and $p_{-(v+1)}(\boldsymbol{R}_\gamma)$, $\Phi_{-(v+1)}(\boldsymbol{R}_\gamma)$, $\chi_{-(v+1)}(\boldsymbol{R}_\gamma)$, $\hat{p}_{-(v+1)}(\boldsymbol{R}_\gamma)$, etc. are solid spherical harmonics of order $-(v+1)$. Expansions (3.6) and (3.7) are precalculated to sufficient orders (see below) by an economical rotation-based algorithm (Section 3.2 of [10]); since these operations are accumulated for individual nodes $\boldsymbol{x}_j \in \mathscr{B}_\gamma$, simultaneous generation of (3.6) and (3.7) is almost as fast as for (3.6) or (3.7) separately. If $\lambda \neq 1$, similar expansions associated with the subtraction tensor (3.5) are also precalculated

$$\frac{3}{4\pi} \sum_{\boldsymbol{x}_j \in \mathscr{B}_\gamma} \frac{[(\boldsymbol{x}_j - \boldsymbol{y}) \cdot \boldsymbol{n}(\boldsymbol{x}_j)\Delta S_j](x_j - y)_k (\boldsymbol{x}_j - \boldsymbol{y})}{\|\boldsymbol{x}_j - \boldsymbol{y}\|^5} = \sum_{v=1}^{\infty} \left[\nabla \times \left(\boldsymbol{R}_\gamma \tilde{\chi}_{-(v+1)}^k \right) + \nabla \tilde{\Phi}_{-(v+1)}^k - \frac{(v-2)R_\gamma^2 \nabla \tilde{p}_{-(v+1)}^k}{2v(2v-1)} + \frac{(v+1)\tilde{p}_{-(v+1)}^k \boldsymbol{R}_\gamma}{v(2v-1)} \right] + \nabla \tilde{\Phi}_{-1}^k. \tag{3.8}$$

Here, three sets of harmonics $\tilde{p}_{-(v+1)}^k$, $\tilde{\Phi}_{-(v+1)}^k$, $\tilde{\chi}_{-(v+1)}^k$ (for $k = 1, 2$ and 3) must be generated. However, this costly operation is optimized (compared to threefold expansions (3.8) for $k = 1, 2$ and 3) by relations between the coefficients in $\tilde{p}_{-(v+1)}^k$, $\tilde{\Phi}_{-(v+1)}^k$ and $\tilde{\chi}_{-(v+1)}^k$ stemming from the symmetry of the subtraction tensor (see Appendix A).

Now, if shell $\mathscr{D}_\delta$ around $\mathscr{B}_\delta \ni \boldsymbol{y}$ and shell $\mathscr{D}_\gamma$ do not overlap, the contribution of patch $\mathscr{B}_\gamma$ to the sums (3.2) can be evaluated at $\boldsymbol{y} \in \mathscr{B}_\delta$ by first re-expanding (3.6) and (3.7) at $\boldsymbol{x}_\delta^o$ in Lamb's regular series

$$\sum_{n=1}^{\infty}\left[\nabla\times(\boldsymbol{R}_\delta\chi_n)+\nabla\Phi_n+\frac{(n+3)R_\delta^2\nabla p_n}{2(n+1)(2n+3)}-\frac{np_n\boldsymbol{R}_\delta}{(n+1)(2n+3)}\right], \tag{3.9}$$

where $\boldsymbol{R}_\delta=\boldsymbol{y}-\boldsymbol{x}_\delta^o$, and $p_n(\boldsymbol{R}_\delta)$, $\Phi_n(\boldsymbol{R}_\delta)$ and $\chi_n(\boldsymbol{R}_\delta)$ are solid harmonics of order n. However, only patches $\mathscr{B}_\gamma$ "sufficiently separated" from $\mathscr{B}_\delta$ are included in this operation, so that the minimal shells $\mathscr{D}_\delta$ and $\mathscr{D}_\gamma$ have enough clearance for sufficient convergence of (3.9), and contributions from all such patches (on S_1+S_2 for the first sum of (3.2), and on S_β only for the second sum (3.2)) are accumulated, using a fast, rotation-based re-expansion algorithm (Section 3.3 of [10]). The cumulative series (3.9) are then transformed to a more efficient form (see Eq. (3.19) of [10])

$$\frac{1}{2}\boldsymbol{R}_\delta\sum_{n=1}^{\infty}p_n(\boldsymbol{R}_\delta)+\sum_{n=0}^{\infty}\sum_{m=-n}^{n}\boldsymbol{H}_{n,m}\left(\frac{R_\delta}{d_\delta^o}\right)^n Y_{n,m}(\boldsymbol{R}_\delta), \tag{3.10}$$

where $\boldsymbol{H}_{n,m}$ are some vector coefficients, and Y_{nm} are surface spherical harmonics, and calculated pointwise for all $\boldsymbol{y}\in\mathscr{B}_\delta$. Similar operations are performed to calculate contributions from all patches $\mathscr{B}_\gamma\subset S_\beta$ "sufficiently separated" from $\mathscr{B}_\delta$ to the subtraction tensor (3.5). The difference is that now there are three sets of harmonics $p_n^k(\boldsymbol{R}_\delta)$, $\Phi_n^k(\boldsymbol{R}_\delta)$, $\chi_n^k(\boldsymbol{R}_\delta)$ and coefficients $\boldsymbol{H}_{n,m}^k$ in (3.9) and (3.10) corresponding to $k=1,2,3$ in (3.8); the symmetry of the subtraction tensor yields some relations between the coefficients in p_n^k, Φ_n^k and χ_n^k (see Appendix A) to optimize reexpansions from (3.8) to (3.9) (compared to the threefold repetition of the procedure) and is also used for more economical pointwise calculations of (3.10).

If patch $\mathscr{B}_\gamma\neq\mathscr{B}_\delta$ is not "sufficiently separated" from $\mathscr{B}_\delta$, but node $\boldsymbol{y}\in\mathscr{B}_\delta$ is "well outside" $\mathscr{D}_\gamma$ (see below for precise definitions), Lamb's singular series (3.6) and (3.7) or (3.8) is used directly to calculate left-hand sides of these equations (again, the symmetry of the subtraction tensor allows us to optimize calculations in (3.8).) Only in rare cases, when $\boldsymbol{y}$ is inside $\mathscr{D}_\gamma$ or is outside but too close to $\mathscr{D}_\gamma$, standard point-to-point summations in the left-hand sides of (3.6) and (3.7) or (3.8) are used.

The evaluation of the first sum in the RHS of (3.3) (minus the self-interaction contribution) on each iteration follows the same logic; we just start from Lamb's singular series

$$\sum_{\boldsymbol{x}_j\in\mathscr{B}_\gamma}\boldsymbol{Q}(\boldsymbol{x}_j)\cdot\boldsymbol{T}(\boldsymbol{x}_j-\boldsymbol{y})\cdot\boldsymbol{n}(\boldsymbol{x}_j)\Delta S_j=\sum_{v=1}^{\infty}\left[\nabla\times\left(\boldsymbol{R}_\gamma\tilde{\chi}_{-(v+1)}\right)+\nabla\tilde{\Phi}_{-(v+1)}-\frac{(v-2)R_\gamma^2\nabla\tilde{p}_{-(v+1)}}{2v(2v-1)}+\frac{(v+1)\tilde{p}_{-(v+1)}\boldsymbol{R}_\gamma}{v(2v-1)}\right]+\nabla\tilde{\Phi}_{-1}, \tag{3.11}$$

and precalculate the solid harmonics $\tilde{p}_{-(v+1)}$, $\tilde{\Phi}_{-(v+1)}$ and $\tilde{\chi}_{-(v+1)}$.

Most of our simulations (Sections 5 and 6) have been performed for two equal drops freely suspended in a shear flow $\boldsymbol{u}_\infty(\boldsymbol{x})=(-\gamma x_2,0,0)$. In this case, a special, symmetric version of the multipole-accelerated code was developed to do boundary-integral calculations (3.2) and (3.3) for $\boldsymbol{y}$ on one of the two drops only, with the mesh and solution continuation to the other drop by central symmetry about the origin; the singular multipole expansions (3.6)–(3.8) are also generated for patches $\mathscr{B}_\gamma$ on one drop only, with a continuation to the other drop. Although slightly more complicated, this symmetric version provides about twofold computational gain compared to the general multipole-accelerated code for two drops.

As in the multipole-accelerated multidrop codes [8,10,11] a very essential feature of the present algorithm is the "economical truncation" of multipole expansions/re-expansions depending on a single precision parameter ε (this parameter is not a deviation from the standard $O(N_\Delta^2)$ non-multipole solution in a rigorous sense, but it does correlate with this deviation). In particular, for fast performance, it is taken into account that the rate of convergence of the re-expansions from Lamb's singular (3.6), (3.7), (3.8), (3.11) to a regular form (3.9) strongly depends on the clearance between the shells $\mathscr{D}_\delta$ and $\mathscr{D}_\gamma$; similarly, the number of terms to be retained in the RHS of (3.6)–(3.8) and (3.11) for pointwise calculations (when necessary) is a

strong function of $\|\boldsymbol{y}-\boldsymbol{x}_\gamma^o\|/d_\gamma^o$. The construction of corresponding truncation bounds for (3.6) and (3.11) parallels that in (3.82)–(3.92) of [10] (just the "blocks" therein replaced by "patches," and the limitation $\mathscr{B}_\gamma \not\subset S_\alpha$ therein replaced by $\mathscr{B}_\gamma \neq \mathscr{B}_\delta$). Expansions/re-expansions associated with the singularity and near-singularity subtractions (3.7) and (3.8), however, are truncated in a slightly different manner, due to the presence of the pointwise factors $\Theta f(\boldsymbol{x}^*)$ and $\Theta \boldsymbol{Q}(\boldsymbol{x}^*)$ in (3.2) and (3.3); the details are described in Appendix B. As $\varepsilon \to 0$, all multipoles are eventually included, which guarantees convergence to the standard non-multipole point-to-point boundary integral calculation. For optimized performance, however, a threshold order $k_o \sim 20$–30 is set to limit the use of multipole expansions/re-expansions: if a truncation bound exceeds k_o, pointwise boundary-integral operations are invoked instead [10]. In particular, this threshold k_o and precision ε define when two patches are "sufficiently separated," and when a node $\boldsymbol{y}$ is "well outside" a shell $\mathscr{D}_\gamma$ in our algorithm. "Precisions" $\varepsilon \sim 10^{-7}$–10^{-8} were typically used in the present problem, which provided about seven-digit actual accuracy (compared to the non-multipole calculation at the same discretization) for the normal fluid velocities. Low-precision runs ($\varepsilon \sim 10^{-3}$–10^{-4}) would be much faster but hardly acceptable, since we are interested in tracking delicate surface separations on the order of 10^{-3}–10^{-4} of the drop radii.

3.3. Dynamical projective mesh

To get convergent results for the surface clearance between two drops in extremely close approach (to $O(10^{-3}$–$10^{-4})$ of the drop radii) and accurately calculate the separation angle in 3D simulations (Section 6), gap-adaptive mesh is required, especially for $Ca \ll 1$ due to film localization. We do not know at present how efficiently this case $Ca \ll 1$ could be handled by mesh restructuring (with local refinements changing the mesh topology); available examples [24] are for considerably larger deformations and capillary numbers than those addressed in the present paper. For two drops in close approach at $Ca \ll 1$, we have developed a special adaptive technique for fixed topology unstructured triangulations based on the new idea of a "dynamical projective mesh."

Suppose some projection center $\boldsymbol{O}_\alpha$ is chosen inside each drop S_α close to another drop. If the projection of the drop mesh onto the unit sphere centered at $\boldsymbol{O}_\alpha$ is an almost uniform mesh ("parametric mesh"), we have desired mesh adaptivity on S_α to the near-contact zone (Fig. 4). Given the velocities $\mathrm{d}\boldsymbol{O}_\alpha/\mathrm{d}t$ of the projection centers, and the normal fluid velocities $q_i = \boldsymbol{u}(\boldsymbol{x}_i)\cdot\boldsymbol{n}(\boldsymbol{x}_i)$ from the boundary-integral solution, it is possible to add a suitable tangential motion on S_α in mesh nodes (without affecting the evolution of drop shapes), so that the parametric mesh remains stationary, to high accuracy. If the parametric mesh was almost uniform at $t = 0$, this property is preserved for the entire simulation. This unit-sphere meshing is used as a parameterization of the deformed surface S_α for normal and curvature calculation, and for surface integration. It is important to stress that no surface interpolations are needed in our method.

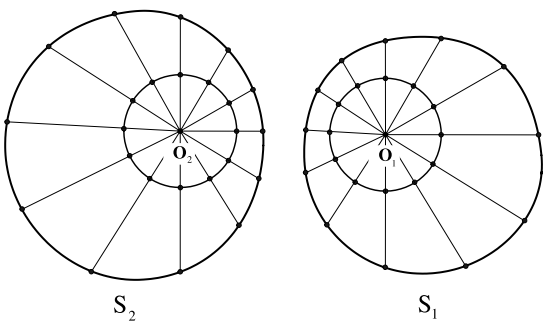

Fig. 4. Gap-adaptive, dynamical projective meshing of drop surfaces (a two-dimensional sketch, not to scale).

The implementation of this idea is technically simple, but non-trivial in some aspects, and follows several consecutive steps:

Step 1: Given the mesh of vertices $\boldsymbol{x}_j$ on deformed surfaces S_α, calculate the "first approximation" $\boldsymbol{X}_\alpha^{\mathrm{c}}$ to surface centroids by a standard trapezoidal rule:

$$\boldsymbol{X}_\alpha^{\mathrm{c}} = \frac{1}{S_\alpha}\int_{S_\alpha} \boldsymbol{x}\,\mathrm{d}S, \quad S_\alpha \approx \sum_{\boldsymbol{x}_j\in S_\alpha} \Delta S_j^o, \quad \int_{S_\alpha} \boldsymbol{x}\,\mathrm{d}S \approx \sum_{\boldsymbol{x}_j\in S_\alpha} \boldsymbol{x}_j \Delta S_j^o, \quad \Delta S_j^o = \frac{1}{3}\sum \Delta S. \tag{3.12}$$

In the definition of ΔS_j^o, the summation is over all flat mesh triangle areas sharing vertex $\boldsymbol{x}_j$, and the relations (3.12) are the same approximations as we used previously [8,10,11].

Step 2: Given an "adaptivity level" L (an integer typically from zero to four, fixed for each run), calculate the projection centers $\boldsymbol{O}_\alpha = \boldsymbol{O}_\alpha^{(L)}$ by a recurrent procedure

$$\begin{aligned} &\boldsymbol{O}_\alpha^{(o)} = \boldsymbol{X}_\alpha^{\mathrm{c}} \quad (\alpha = 1,2),\\ &\boldsymbol{O}_\alpha^{(k)} = \boldsymbol{X}_\alpha^{\mathrm{c}} + \frac{a_\alpha^2\left(\boldsymbol{O}_{3-\alpha}^{(k-1)} - \boldsymbol{X}_\alpha^{\mathrm{c}}\right)}{\left\|\boldsymbol{O}_{3-\alpha}^{(k-1)} - \boldsymbol{X}_\alpha^{\mathrm{c}}\right\|^2} \quad (\alpha = 1,2;\ k = 1,2\ldots L), \end{aligned} \tag{3.13}$$

where a_α are non-deformed drop radii. Relations (3.13) simply mean that we first put $\boldsymbol{O}_\alpha^{(o)}$ in the drop centroids $\boldsymbol{X}_\alpha^{\mathrm{c}}$, then invert each $\boldsymbol{O}_\alpha^{(k)}$ about another sphere of radius a_β ($\beta \neq \alpha$) centered at $\boldsymbol{X}_\beta^{\mathrm{c}}$ to obtain $\boldsymbol{O}_\beta^{(k+1)}$, and so on (Fig. 5). The higher L, the closer each projection center is to another surface, thereby increasing the adaptivity (interestingly, in the limit $L \to \infty$, $\boldsymbol{O}_\alpha$ would coincide with the poles of the bispherical coordinate system for two spheres of radii a_1, a_2 centered at $\boldsymbol{X}_1^{\mathrm{c}}$, $\boldsymbol{X}_2^{\mathrm{c}}$). However, large L would lead to overadaptivity (and difficulties when the non-deformed spheres start overlapping) and must be avoided. Level $L = 0$ yields non-adaptive meshes. The values of $L = 1$ and $2 \leqslant L \leqslant 4$ give "weakly adaptive" and "moderately adaptive" meshes, respectively. The method based on (3.13) will be referred to as "mesh adaptation 1" (MA1). In most of our shear flow simulations for equal drops ($a_1 = a_2 = a$), an improved version was used (MA2): when $\|\boldsymbol{X}_2^{\mathrm{c}} - \boldsymbol{X}_1^{\mathrm{c}}\| < 2a$, then $\|\boldsymbol{X}_2^{\mathrm{c}} - \boldsymbol{X}_1^{\mathrm{c}}\|/2$ is used instead of a in (3.13). This modification allows us to avoid overadaptivity (and, accordingly, too small time steps) at the compression stage of two-drop relative motion; in typical 3D simulations, we have found adaptivity to be equally important at the tensile stage ($\|\boldsymbol{X}_2^{\mathrm{c}} - \boldsymbol{X}_1^{\mathrm{c}}\| > 2a$), before drop separation. Both the MA1 and MA2 schemes lead to some undesirable loss of local resolution close to separation (when $\|\boldsymbol{X}_2^{\mathrm{c}} - \boldsymbol{X}_1^{\mathrm{c}}\| > 2a$, but the surface clearance is still extremely small, see Section 5). In the present shear-flow simulations (when only relative motion up to separation is of interest), this drawback is overcome by using a better yet version MA3: as soon as the center-to-center distance $\|\boldsymbol{X}_2^{\mathrm{c}} - \boldsymbol{X}_1^{\mathrm{c}}\|$ has reached $2a$ for the first time, then $\|\boldsymbol{X}_2^{\mathrm{c}} - \boldsymbol{X}_1^{\mathrm{c}}\|/2$ is used instead of a in (3.13) for the rest of the simulation. This modification maintains an almost constant adaptivity for the entire near-contact motion, from close approach to separation. The preferred scheme MA3, though,

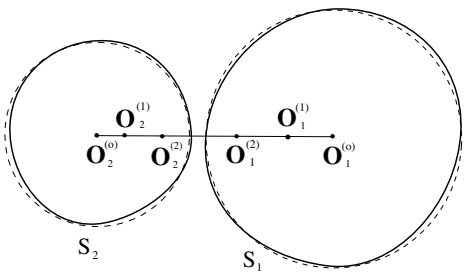

Fig. 5. A recurrent procedure for constructing projection centers. Dashed lines correspond to non-deformed spheres.

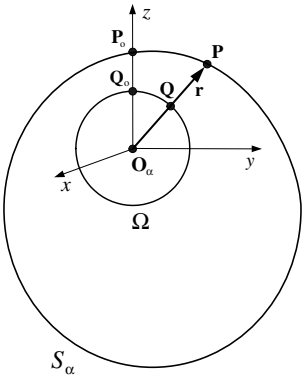

Fig. 6. Curvature and normal vector calculation on a projective mesh.

was used only in a few, most recent runs; the majority of the shear flow calculations in Sections 5 and 6 are based on MA1/MA2. Additional flexibility could be achieved by using slightly contracted radii $\hat{a}_\alpha$ instead of a_α in all schemes MA1–MA3 to allow for a continuous spectrum of mesh adaptivities, although such an option was not used in the present calculations.

Step 3: Calculate normals $\boldsymbol{n}(\boldsymbol{x}_j)$ and mean curvatures $k(\boldsymbol{x}_j) = \frac{1}{2}(k_1 + k_2)$ in mesh nodes on S_α using the parametric unit sphere meshing. Let $\boldsymbol{P}_o \in S_\alpha$ be the node of interest, and $\boldsymbol{Q}_o$ be the projection of $\boldsymbol{P}_o$ onto the unit sphere Ω centered at $\boldsymbol{O}_\alpha$ (Fig. 6). Let (x, y, z) be local coordinates centered at $\boldsymbol{O}_\alpha$ with the z-axis along $\boldsymbol{O}_\alpha\boldsymbol{P}_o$ (an arbitrary rotation about $\boldsymbol{O}_\alpha\boldsymbol{P}_o$ is insignificant). For a close drop surface point $\boldsymbol{P} \approx \boldsymbol{P}_o$, the (x, y)-coordinates of the projection $\boldsymbol{Q}$ of point $\boldsymbol{P}$ (Fig. 6) can be considered as local parameterization of the drop surface. The surface equation is $\boldsymbol{r} = r(x, y)\boldsymbol{\rho}$, where $\boldsymbol{r} = \boldsymbol{P} - \boldsymbol{O}_\alpha$, $r = \|\boldsymbol{r}\|$ and $\boldsymbol{\rho} = \boldsymbol{O}_\alpha\boldsymbol{Q} \approx (x, y, 1 - (x^2 + y^2)/2)$. The normal vector

$$\boldsymbol{n}(\boldsymbol{P}_o) = \left(\frac{\partial \boldsymbol{r}}{\partial x} \times \frac{\partial \boldsymbol{r}}{\partial y}\right) \Bigg/ \left\|\frac{\partial \boldsymbol{r}}{\partial x} \times \frac{\partial \boldsymbol{r}}{\partial y}\right\| \quad (x = y = 0), \tag{3.14}$$

in coordinates (x, y, z) takes the form

$$\boldsymbol{n}(\boldsymbol{P}_o) = \frac{1}{D}\left(-\frac{\partial R}{\partial x}, -\frac{\partial R}{\partial y}, 1\right), \quad D = \left[1 + \left(\frac{\partial R}{\partial x}\right)^2 + \left(\frac{\partial R}{\partial y}\right)^2\right]^{1/2} \quad (x = y = 0), \tag{3.15}$$

where $R = \ln r$.

The covariant metric tensor at $x = y = 0$ is

$$g_{xx} = r^2\left[1 + \left(\frac{\partial R}{\partial x}\right)^2\right], \quad g_{yy} = r^2\left[1 + \left(\frac{\partial R}{\partial y}\right)^2\right], \quad g_{xy} = r^2\frac{\partial R}{\partial x}\frac{\partial R}{\partial y}. \tag{3.16}$$

The coefficients of the second quadratic form at $x = y = 0$ are

$$\begin{aligned} B_{xx} &= -\boldsymbol{n}(\boldsymbol{P}_o) \cdot \frac{\partial^2 \boldsymbol{r}}{\partial x^2} = r\left[1 + \frac{\partial R}{\partial x} - \frac{\partial^2 R}{\partial x^2}\right] \Big/ D, \\ B_{xy} &= -\boldsymbol{n}(\boldsymbol{P}_o) \cdot \frac{\partial^2 \boldsymbol{r}}{\partial x \partial y} = r\left[\frac{\partial R}{\partial x}\frac{\partial R}{\partial y} - \frac{\partial^2 R}{\partial x \partial y}\right] \Big/ D, \\ B_{yy} &= -\boldsymbol{n}(\boldsymbol{P}_o) \cdot \frac{\partial^2 \boldsymbol{r}}{\partial y^2} = r\left[1 + \frac{\partial R}{\partial y} - \frac{\partial^2 R}{\partial y^2}\right] \Big/ D. \end{aligned} \tag{3.17}$$

The average curvature at $\boldsymbol{P}_o$ can now be calculated by standard rules

$$k(\boldsymbol{P}_o) = \frac{1}{2}(B_{xx}g_{yy} + B_{yy}g_{xx} - 2B_{xy}g_{xy})/(g_{xx}g_{yy} - g_{xy}^2). \tag{3.18}$$

To implement (3.15)–(3.18), a local approximation is used

$$R(x,y) \approx R(0,0) + Ax + By + Cx^2 + Dxy + Ey^2 \tag{3.19}$$

with the coefficients A, B, C, D and E found by least-square fitting of (3.19) to the values of $R(x,y)$ for the nodes (typically, six) directly connected to $\boldsymbol{P}_o$. The formulation (3.15)–(3.19) in terms of $R = \ln r$ is designed to considerably reduce numerical errors when the projection center $\boldsymbol{O}_\alpha$ is close to the surface S_α and r has a large variation over S_α. Our tests for 3D ellipsoids (with almost uniform parametric mesh and random projection centers inside the surface) also showed that the new method, although specific for the problem, considerably reduces errors in the curvature calculation (about 2–5 times), compared to the best paraboloid algorithm [29], especially for slightly deformed shapes. Unlike in the best paraboloid algorithm, the present calculations of $\boldsymbol{n}$ and k are non-iterative. In one test run, we used high-order surface approximation instead of (3.19) to calculate curvatures and normals. Namely, $R(x,y)$ was locally approximated by a fourth-degree polynomial in x,y, with prescribed $R(0,0)$ and the remaining 14 coefficients found by least-square fitting to the values of $R(x,y)$ at 15–18 nodes forming two mesh layers around $\boldsymbol{P}_o$. Although a big generic improvement for smooth surfaces, such modification was found to be of little help in the present close-contact calculations at $Ca \to 0$ (Section 5).

Step 4: Calculate the "surface area" ΔS_j associated with node $\boldsymbol{x}_j \in S_\alpha$, to be used in surface integrations (3.1). The integral (3.1) over the drop surface can be transformed to the integral over the unit sphere Ω centered at $\boldsymbol{O}_\alpha$

$$\int_{S_\alpha} \varphi(\boldsymbol{x})\,\mathrm{d}S = \int_{\|\boldsymbol{Q}-\boldsymbol{O}_\alpha\|=1} \frac{\varphi(\boldsymbol{P})r^3\,\mathrm{d}\Omega_Q}{\boldsymbol{r}\cdot\boldsymbol{n}(\boldsymbol{P})}, \quad \boldsymbol{r} = \boldsymbol{P} - \boldsymbol{O}_\alpha, \tag{3.20}$$

where $\boldsymbol{Q}$ is the image of $\boldsymbol{P} \in S_\alpha$ on the unit sphere (Fig. 6), and $d\Omega_Q$ is the unit sphere surface element. Applying the usual trapezoidal rule to the RHS of (3.20) yields

$$\Delta S_j = \frac{1}{3}\frac{r^3}{\boldsymbol{r}\cdot\boldsymbol{n}(\boldsymbol{x}_j)}\sum \Delta\Omega, \quad \boldsymbol{r} = \boldsymbol{x}_j - \boldsymbol{O}_\alpha, \tag{3.21}$$

where the summation is over all areas $\Delta\Omega$ of flat triangles of the parametric mesh sharing the image of node $\boldsymbol{x}_j$. Using (3.1), (3.20) and (3.21) has an obvious analogy in the one-dimensional case: instead of direct integration on a highly non-uniform mesh, it is usually much better, in terms of accuracy, to construct a mapping function (accounting for steep behaviour of an integrand) and calculate a modified integral on a uniform mesh in the new variable. In particular, using (3.1), (3.20) and (3.21), we achieved excellent drop volume conservation in dynamical simulations (without any forcing), unattainable with other integration methods.

Step 5: Solve the boundary-integral problem for a given configuration of nodes $\boldsymbol{x}_j \in S_\alpha$, and calculate the fluid normal velocities $q_j = \boldsymbol{u}(\boldsymbol{x}_j)\cdot\boldsymbol{n}(\boldsymbol{x}_j)$. With curvatures and normals from Step 3, and ΔS_j from Step 4, we discretize the boundary-integral equation (2.7) (Section 3.1) and solve it by the minimal residual techniques (the same version as in [8]) using our multipole-accelerated scheme. In generating patches (Section 3.2), it is advantageous to use the same centers $\boldsymbol{O}_\alpha$ as for the projective mesh. At $\lambda \neq 1$, the surface centroids $\boldsymbol{x}_\alpha^c$ required for calculating rigid-body projections $\boldsymbol{w}'$ in (2.7) (see (11)–(15) of [29]) are found by integration rules (3.1), (3.20) and (3.21), rather than by less accurate (3.12).

Step 6 (A version of "passive mesh stabilization"): Add a suitable tangential motion in mesh nodes on each S_α, to make the parametric mesh to remain stationary. We wish to move the mesh nodes $\boldsymbol{x}_j \in S_\alpha$ with

velocities $\boldsymbol{V}_j = \mathrm{d}\boldsymbol{x}_j/\mathrm{d}t$, so that the unit vectors $(\boldsymbol{x}_j - \boldsymbol{O}_\alpha)/\|\boldsymbol{x}_j - \boldsymbol{O}_\alpha\|$ of the parametric mesh would remain stationary, requiring

$$\frac{\mathrm{d}}{\mathrm{d}t}(\boldsymbol{x}_j - \boldsymbol{O}_\alpha) \,||\, \boldsymbol{x}_j - \boldsymbol{O}_\alpha. \tag{3.22}$$

However, the velocities $\boldsymbol{V}_j$ are subject to the constraints $\boldsymbol{V}_j \cdot \boldsymbol{n}(\boldsymbol{x}_j) = q_j$ provided by the boundary-integral solution (Step 5). Satisfying both requirements yields

$$\boldsymbol{V}_j = \dot{\boldsymbol{O}}_\alpha + \frac{q_j - \dot{\boldsymbol{O}}_\alpha \cdot \boldsymbol{n}(\boldsymbol{x}_j)}{(\boldsymbol{x}_j - \boldsymbol{O}_\alpha)\cdot \boldsymbol{n}(\boldsymbol{x}_j)}(\boldsymbol{x}_j - \boldsymbol{O}_\alpha), \quad \dot{\boldsymbol{O}}_\alpha = \frac{\mathrm{d}\boldsymbol{O}_\alpha}{\mathrm{d}t}. \tag{3.23}$$

It remains to discuss how to calculate $\dot{\boldsymbol{O}}_\alpha$. Differentiating (3.13) (or its MA2–MA3 modification) with respect to time yields recurrent relations for $\mathrm{d}\boldsymbol{O}_\alpha^{(k)}/\mathrm{d}t$ in terms of $\boldsymbol{X}_\alpha^{\mathrm{c}}$, $\mathrm{d}\boldsymbol{X}_\alpha^{\mathrm{c}}/\mathrm{d}t$, $\boldsymbol{O}_{3-\alpha}^{(k-1)}$ and $d\boldsymbol{O}_{3-\alpha}^{(k-1)}/\mathrm{d}t$, so the problem is reduced to calculating $\mathrm{d}\boldsymbol{X}_\alpha^{\mathrm{c}}/\mathrm{d}t$ from (3.12). Since a flat triangle area ΔS is a known function of its vertices, then, through (3.12), $\mathrm{d}\boldsymbol{X}_\alpha^{\mathrm{c}}/\mathrm{d}t$ can be expressed in terms of all $\boldsymbol{x}_j \in S_\alpha$ and $\mathrm{d}\boldsymbol{x}_j/\mathrm{d}t$. A difficulty is that the velocities $\mathrm{d}\boldsymbol{x}_j/\mathrm{d}t$ themselves are unknown. However, for sufficient triangulations, the centroid $\boldsymbol{X}_\alpha^{\mathrm{c}}$ is primarily a function of the drop *shape* (rather than of artificial positions of the nodes $\boldsymbol{x}_j \in S_\alpha$), and $\mathrm{d}\boldsymbol{X}_\alpha^{\mathrm{c}}/\mathrm{d}t$ is almost insensitive to tangential components of the velocities $\mathrm{d}\boldsymbol{x}_j/\mathrm{d}t$. So, an approximation

$$\frac{\mathrm{d}\boldsymbol{x}_j}{\mathrm{d}t} \approx q_j\boldsymbol{n} + (\boldsymbol{I} - \boldsymbol{nn})\boldsymbol{V}_j', \quad \boldsymbol{n} = \boldsymbol{n}(\boldsymbol{x}_j), \tag{3.24}$$

where $\boldsymbol{V}_j'$ is the velocity (determined by (3.23)) from the preceding time step, is enough for very accurate calculation of $\mathrm{d}\boldsymbol{X}_\alpha^{\mathrm{c}}/\mathrm{d}t$. Consecutive steps 1–6 determine, for a given configuration of nodes $\boldsymbol{x}_j \in S_\alpha$, the velocities (3.23) to update the drop shapes. The system of differential equations $\mathrm{d}\boldsymbol{x}_j/\mathrm{d}t = \boldsymbol{V}_j(\boldsymbol{x}_1, \boldsymbol{x}_2, \ldots)$ was advanced by a second-order RK scheme. At $t = 0$, the two drops were assumed to be non-deformed, with prescribed center-to-center offsets; the initial node positions $\boldsymbol{x}_j \in S_\alpha$ were analytically calculated by projecting an almost uniform parametric mesh onto the spherical surface S_α. The maximum-to-minimum mesh edge ratio for a parametric mesh was always within 1.19, and the nodes $(\boldsymbol{x}_j - \boldsymbol{O}_\alpha)/\|\boldsymbol{x}_j - \boldsymbol{O}_\alpha\|$ of the parametric mesh remained stationary to about five digits(!) in each run, while the surface meshes $\{\boldsymbol{x}_j \in S_\alpha\}$ were highly non-uniform, with maximum-to-minimum mesh edge ratio on the order of 10 for close contact in most runs.

3.4. Choice of the time step

Three-dimensional simulations of two-drop close approach and separation at $Ca \ll 1$ require a very large total number of time steps (Section 5) due to tight stability limitations, so an economical time-step strategy is of primary importance. In physical units, the time step Δt is subject to the usual restriction $\Delta t \leqslant K_{\Delta t}\mu_e \Delta x/\sigma$ (where Δx is the minimum distance between directly connected mesh nodes, and $K_{\Delta t} = \mathrm{O}(1)$ is a numerical factor), as was first noticed [30] in one-drop calculations at finite deformations. For two drops in close approach, this criterion (with optimal $K_{\Delta t}$) must be tightened (otherwise, the calculation of the surface clearance, $h_{\min}$, suffers from numerical instability). We used a new, semi-empirical rule suitable for small deformations

$$\Delta t = \frac{K_{\Delta t}\mu_e}{\sigma}\min(\Delta x, 0.7\Delta x_2), \tag{3.25}$$

where

$$\Delta x_2 = \min_{i,j} \big|\big|\boldsymbol{x}_j - \boldsymbol{x}_i\big|\big|, \quad \boldsymbol{x}_i \in S_1, \;\; \boldsymbol{x}_j \in S_2 \tag{3.26}$$

is the minimum distance between mesh nodes on different surfaces, but *excluding* pairs (i,j), for which $\boldsymbol{x}_j$ is the node on S_2 closest to $\boldsymbol{x}_i$, or $\boldsymbol{x}_i$ is the node on S_1 closest to $\boldsymbol{x}_j$, or both. This exclusion is very substantial and due to near-singularity subtractions (3.2), since the nearest node $\boldsymbol{x}^*$ makes practically zero contribution to the RHS of (3.2) after subtraction; the coefficient 0.7 is an empirical correction. Another small empirical correction, for drops in close approach, was to reduce the time step (3.25) by 10%, once the β-angle between the line-of-centers and the flow (or gravity) direction exceeded $\approx$1.5 rad, as it was observed that the tensile stage of two-drop motion is more subject to numerical instability. For widely separated drops, (3.25) becomes the usual limitation $\Delta t = K_{\Delta t}\mu_e \Delta x/\sigma$, but our numerical factors $K_{\Delta t}$ appear to be larger than those used with other codes. For $\lambda = 1$, we found $K_{\Delta t} = 3.5$ appropriate (compared to $K_{\Delta t} = 0.5$ in large-deformation calculations [1,6,7] for 2–12 drops; the difference is likely due to "springs" used in the algorithms [1,6,7] to stabilize the mesh). For moderately high $\lambda = 4$–10, our values of $K_{\Delta t}$ are even relaxed 2–2.5 times; for $\lambda \ll 1$, however, much smaller $K_{\Delta t} \ll 3.5$ are needed in close approach (e.g., $K_{\Delta t} = 1.05$ for $\lambda = 0.25$), making those runs most difficult (Section 6). For drops in close contact and a locally isotropic mesh on S_α, with approximately equilateral mesh triangles, the second term in (3.25), $0.7\Delta x_2$, is, on average, $0.44\Delta x$, and so it presents a little additional restriction. Had we taken *all* pairs (i,j) in the definition (3.26), the limitation (3.25) would be much tighter, making most of the results in Sections 5 and 6 not feasible. The form (3.25) is much more economical in close approach than the one we used previously [29].

4. Asymptotic techniques

Even with multipole acceleration, obtaining convergent 3D boundary-integral results for two drops in close contact at $Ca \to 0$ is numerically very difficult (Sections 5 and 6). As an alternative, an asymptotic technique was developed [22] based on the idea of matched asymptotic expansions. On the lengthscale of the drop size, the drops are considered as non-deformed fluid spheres, and they approach contact in a finite time because the hydrodynamic resistance coefficient has an integrable singularity $\sim h^{-1/2}$ [18,20], as the surface clearance $h \to 0$. On the deformation lengthscale, however, there is a small non-uniform gap between the drops that evolves under the action of hydrodynamic forces. An additional effect of van der Waals forces [22] was disabled, for simplicity, in the present study; without van der Waals attractions, deformable surfaces never touch [16,17]. Assuming that tangential motion is practically unaffected by small deformation (which is fully confirmed by the boundary-integral tests [22]), the outer solution for spherical drops in apparent contact provides the time-dependent contact force acting along the line of centers. This force serves as a lubrication force to close local, integro-differential equations for the thin film in the gap. Even though the whole problem is 3D, it was shown [22] that, to the leading order in $Ca \ll 1$, the film must be locally axisymmetric, which greatly simplifies the analysis. The initial conditions for the inner solution were provided by matching with the outer trajectory for spherical drops, and the thin-film equations (which are numerically very stiff) for fully mobile surfaces were solved by a special absolutely stable method [22]. This approach has been systematically applied to coalescence efficiency calculations in gravity-induced and shear-induced motions [22,23].

The techniques and results [22,23] are substantially limited by $\lambda \gg |\ln Ca| Ca^{1/2}$ and $\lambda \ll Ca^{-1/2}$, so that neither small nor large viscosity ratios are covered. In the present work, we extended the asymptotic techniques to 3D collisions of highly viscous drops ($\lambda \gg 1$). Not only the thin film algorithm is necessarily different, but the matching condition with the outer trajectory takes a new form, as detailed below. The key assumption is that the tangential motion of drops is still unaffected by small deformations.

For the gravity-induced motion of two drops in a quiescent liquid (Fig. 7), the hydrodynamical forces acting on two spherical drops in apparent contact are

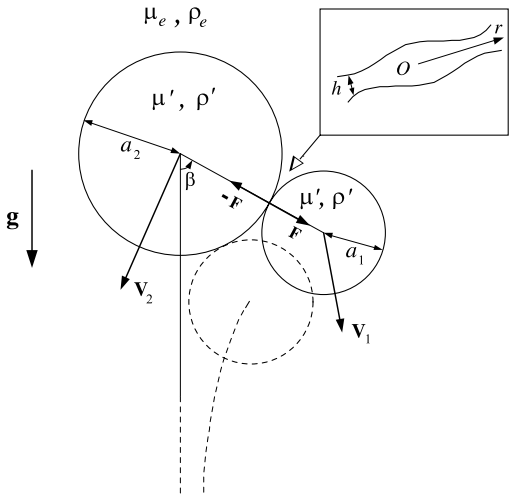

Fig. 7. A schematic for gravity-induced motion of two spherical drops in apparent contact. A close-up of the inner region, with small deformation, is also shown.

$$\begin{aligned}\boldsymbol{F}_1 &= -6\pi\mu_e a_1\left[\Lambda^t_{12}\boldsymbol{V} + T^t_{11}(\boldsymbol{V}_1-\boldsymbol{V}_2)^{\perp} + T^t_{12}\boldsymbol{V}_2^{\perp}\right] + \boldsymbol{F},\\ \boldsymbol{F}_2 &= -6\pi\mu_e a_2\left[\Lambda^t_{22}\boldsymbol{V} + T^t_{21}(\boldsymbol{V}_2-\boldsymbol{V}_1)^{\perp} + T^t_{22}\boldsymbol{V}_2^{\perp}\right] - \boldsymbol{F},\end{aligned} \tag{4.1}$$

where $\boldsymbol{V}$ is the common velocity of the drops along the line of centers, $\perp$ denotes the vector component normal to the line of centers, $\boldsymbol{V}_1$ and $\boldsymbol{V}_2$ are the velocities of geometric centers of spheres, and $\boldsymbol{F}$ and $-\boldsymbol{F}$ are contact forces acting along the line of centers. The resistance coefficients Λ^t_{12} and Λ^t_{22} for the aggregate and the T^t_{ij} coefficients in the limit of touching are known from the solutions [32,33], respectively. The force balances $\boldsymbol{F}_i + \frac{4}{3}\pi a_i^3\Delta\rho\boldsymbol{g} = \boldsymbol{0}$ yield the contact force

$$F(\beta) = \frac{4}{3}\pi\frac{a_1a_2\left(a_2^2\Lambda^t_{12} - a_1^2\Lambda^t_{22}\right)}{a_2\Lambda^t_{22} + a_1\Lambda^t_{12}}\Delta\rho g\cos\beta, \tag{4.2}$$

and the dynamics of the β-angle between the centerline and the vertical for the contact motion [22]

$$\frac{\mathrm{d}\beta}{\mathrm{d}t} = \kappa T\sin\beta, \quad \kappa = \frac{2}{9}\frac{\Delta\rho g a_2^2}{(a_1+a_2)\mu_e}, \quad T = \frac{T^t_{12} - k^2T^t_{22}}{T^t_{11}T^t_{22} + T^t_{21}T^t_{12}}, \tag{4.3}$$

where $k = a_1/a_2$ is the size ratio. Integrating (4.3) gives $F(\beta(t))$ as an explicit function of time.

For two freely suspended drops in a shear flow (Fig. 8), $\boldsymbol{u}_\infty = (-\gamma x_2, 0, 0)$, the center-to-center director $\boldsymbol{p}$ from sphere 2 to sphere 1 is characterized by two angles β and θ

$$p_1 = \sin\theta\cos\beta, \quad p_2 = \sin\theta\sin\beta, \quad p_3 = \cos\theta, \tag{4.4}$$

and the contact force has the form [23]

$$F(\beta,\theta) = 3\pi\mu_e a_1(a_1+a_2)D^*\gamma\sin^2\theta\sin\beta\cos\beta, \tag{4.5}$$

where

$$D^* = \frac{\lambda+\frac{2}{3}}{\lambda+1}\frac{D^t_1\Lambda^t_{22} + D^t_2\Lambda^t_{12}}{\Lambda^t_{22} + k\Lambda^t_{12}} \tag{4.6}$$

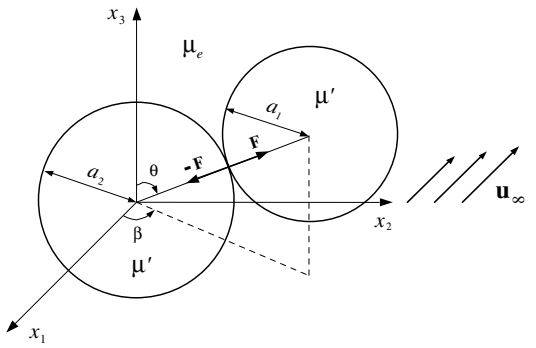

Fig. 8. A schematic for shear-induced motion of two spherical drops in apparent contact.

and the hydrodynamical coefficients D_1^t and D_2^t are obtained from the bispherical coordinate solution [34] in the limit of touching. For equal drops $a_1 = a_2$, the values of $D^*(\lambda)$ are tabulated [35]. The dynamics of contact motion is described by

$$\frac{\mathrm{d}\beta}{\mathrm{d}t} = \gamma\left[\left(1-\frac{B^t}{2}\right)\sin^2\beta + \frac{B^t}{2}\cos^2\beta\right], \quad \frac{\mathrm{d}\theta}{\mathrm{d}t} = -\gamma(1-B^t)\sin\theta\cos\theta\sin\beta\cos\beta, \tag{4.7}$$

where B^t is the hydrodynamic mobility function in the zero-gap limit, found from the solutions [34,35]. Again, solving (4.7) yields the contact force $F(\beta(t),\theta(t))$ as a function of time.

To non-dimensionalize the thin-film equations (which have different length and velocity scales than for the global motion), a characteristic film radius b is introduced

$$\pi b^2\sigma = \Delta\rho g R^4 \tag{4.8}$$

for the gravity-induced motion [22] and

$$\pi b^2\sigma = 8\gamma\mu_e R^3 \tag{4.9}$$

for the shear-flow problem, where $R = a_1a_2/(a+a_2)$ is the reduced radius. The assumption [22,23] of high interfacial mobility is not applicable for $\lambda Ca^{1/2} \geqslant \mathrm{O}(1)$, and so a more general form of the continuity equation [21] is used herein, to account for the parabolic portion of the velocity profile in the gap.

Introducing non-dimensional variables for the film thickness $\tilde{h}$, radial coordinate $\tilde{r}$ from the film center, pressure $\tilde{p}$, interfacial tangential stress $\tilde{f}$, interfacial velocity $\tilde{u}$ (in the reference frame moving with the gap) and time $\tilde{t}$ by the relations

$$h = \frac{b^2}{R}\tilde{h}, \quad r = b\tilde{r}, \quad p = \frac{\sigma}{2R}\tilde{p}, \quad f = \frac{b\sigma}{2R^2}\tilde{f}, \quad u = \frac{1}{2}\frac{b^2}{R^2}\frac{\sigma}{\mu'}\tilde{u}, \quad t = \frac{2R^2}{b}\frac{\mu'}{\sigma}\tilde{t}, \tag{4.10}$$

the thin-film equations take the form:

Normal stress balance

$$\tilde{p} = 2 - \frac{1}{\tilde{r}}\frac{\partial}{\partial\tilde{r}}\left(\tilde{r}\frac{\partial\tilde{h}}{\partial\tilde{r}}\right). \tag{4.11}$$

Momentum balance

$$\tilde{f} = -\frac{\tilde{h}}{2}\frac{\partial\tilde{p}}{\partial\tilde{r}}. \tag{4.12}$$

Local boundary integral

$$\tilde{u}(\tilde{r}) = \int_0^\infty \phi(\tilde{r}', \tilde{r}) \tilde{f}(\tilde{r}')\, \mathrm{d}\tilde{r}'. \tag{4.13}$$

Mass continuity

$$\frac{\partial \tilde{h}}{\partial \tilde{t}} + \frac{1}{\tilde{r}} \frac{\partial}{\partial \tilde{r}} \left[\tilde{r} \tilde{h} \bar{u}\right] = 0, \quad \bar{u} = \tilde{u} - \frac{\tilde{\lambda} \tilde{h}^2}{12} \frac{\partial \tilde{p}}{\partial \tilde{r}}. \tag{4.14}$$

Integral force balance

$$\int_0^\infty \tilde{p} \tilde{r}\, \mathrm{d}\tilde{r} = Q, \tag{4.15}$$

where

$$\phi(\tilde{r}', \tilde{r}) = \frac{1}{2\pi} \frac{\tilde{r}'}{\left(\tilde{r}^2 + \tilde{r}'^2\right)^{1/2}} \int_0^\pi \left[1 - \frac{2\tilde{r}\tilde{r}' \cos\theta}{\tilde{r}^2 + \tilde{r}'^2}\right]^{-1/2} \cos\theta\, \mathrm{d}\theta, \tag{4.16}$$

$$\tilde{\lambda} = \lambda b/R \sim \lambda Ca^{1/2}, \tag{4.17}$$

$$Q(\beta) = \alpha \cos\beta, \quad \alpha = \frac{4}{3}\pi \frac{(k+1)^3}{k^2} \frac{\Lambda_{12}^t - k^2 \Lambda_{22}^t}{\Lambda_{22}^t + k\Lambda_{12}^t} \tag{4.18}$$

for gravity-induced motion [22] and

$$Q(\beta, \theta) = \frac{3\pi}{8} \frac{(1+k)^3}{k} D^* \sin^2\theta \sin\beta \cos\beta \tag{4.19}$$

for shear-induced motion. In [22,23], $\tilde{\lambda} = 0$ was assumed.

Eqs. (4.11)–(4.15) must be solved simultaneously with the contact-motion equation (4.3) (or (4.7)), and the initial conditions $\tilde{h}(0, \tilde{r})$, β_o (or β_o and θ_o) are required for the film profile and angle β (or β and θ) at $\tilde{t} = 0$. These values must match the corresponding quantities from the outer relative trajectory for spherical drops. Accordingly, we start from some large non-dimensional separation $\tilde{h}_o \gg 1$ (such that $h_o/a_i \ll 1$) and non-deformed film shape $\tilde{h} = \tilde{h}_o + \tilde{r}^2/2$ at $\tilde{t} = 0$, since for $\tilde{h}_o \gg 1$ deformation is still unimportant. The choice of β_o (and θ_o) is less obvious. Let β_c (and θ_c) be the "collision angles," i.e., the values of β (and θ) achieved by the outer trajectory at apparent contact; the values of β_c (and θ_c) are provided by standard trajectory analysis for separated spherical drops, given an initial configuration.

To link β_o (and θ_o) with β_c (and θ_c), we simplify the equations of relative motion for spherical drops approaching contact. The dimensional lubrication force between two highly viscous, nearly touching fluid spheres is known to be asymptotically [19,20]

$$-6\pi\mu_e \frac{R^2}{h_{\mathrm{cen}}} \Phi(p) \frac{\mathrm{d}h_{\mathrm{cen}}}{\mathrm{d}t}, \quad p = \lambda \left(\frac{2h_{\mathrm{cen}}}{R}\right)^{1/2}, \quad h_{\mathrm{cen}} = h|_{r=0} \ll a_i, \tag{4.20}$$

where $\Phi(p)$ has an exact expression [19]

$$\Phi(p) = 32p \sum_{n=1}^{\infty} \frac{n(n+1)}{[4n(n+1) - 3]^2 [(2n+1)p + 6]}. \tag{4.21}$$

(a closed form in terms of the logarithmic derivative of the gamma-function is also possible). Equating (4.20) to the contact force (4.2) or (4.5), and integrating from $h_{\mathrm{cen}} = 0$ to $h_{\mathrm{cen}} = h_o$ yields

$$12\pi\mu_e R^2 I = \int_{\beta_o}^{\beta_c} \frac{F\mathrm{d}\beta}{\mathrm{d}\beta/\mathrm{d}t}, \tag{4.22}$$

where

$$I = \int_0^{p_o} \frac{\Phi(p)}{p}\mathrm{d}p = 32\sum_{n=1}^{\infty} \frac{n(n+1)}{[4n(n+1)-3]^2(2n+1)} \ln\left[1+\frac{(2n+1)p_o}{6}\right] \tag{4.23}$$

and $p_o = \lambda(2h_o/R)^{1/2}$; the derivative $\mathrm{d}\beta/\mathrm{d}t$ in (4.22) is taken from (4.3) or (4.7).

For gravity-induced motion

$$p_o = \lambda\left[\frac{9}{\pi}\frac{k^2}{(1-k^2)(1+k)^2}\frac{\lambda+\frac{2}{3}}{\lambda+1}Ca\,\tilde{h}_o\right]^{1/2}, \tag{4.24}$$

where Ca is defined in (2.8), and (4.22) is easily solved for β_o using (4.2) and (4.3):

$$\sin\beta_o = \sin\beta_c \exp\left[-\frac{2kIT\left(\Lambda_{22}^t + k\Lambda_{12}^t\right)}{(1+k)^3\left(\Lambda_{12}^t - k^2\Lambda_{22}^t\right)}\right]. \tag{4.25}$$

For shear-induced motion

$$p_o = \lambda\sqrt{\frac{8}{\pi}Ca\,\tilde{h}_o} \tag{4.26}$$

with the capillary number defined in (2.9). To get the relation between (β_o, θ_o) and (β_c, θ_c), the system (4.7) may be integrated backwards from $\beta = \beta_c$, until (4.22) is satisfied. For outer relative trajectories lying in the plane of shear $\theta \equiv \pi/2$ (the case considered in the numerical examples of Sections 5 and 6), a simple analytical form is obtained

$$\ln\frac{1-(1-B^t)\cos 2\beta_c}{1-(1-B^t)\cos 2\beta_o} = \frac{8kI(1-B^t)}{(1+k)^3 D^*}. \tag{4.27}$$

A different matching strategy [22] was based on calculating the "collision time" required for a spherical drop trajectory to reach contact from a nearly touching configuration, assuming $F = \text{const.}$ in this estimation. The new form (4.22) takes into account that, during an initial approach of highly viscous spherical drops, angles β and θ, and the contact force may have substantial variations due to slow film drainage; besides, we use a more general lubrication form (4.20) not limited to $p \ll 1$. For $\lambda Ca^{1/2} \ll 1$, both strategies yield practically identical results in the range $\tilde{h} \leqslant \mathrm{O}(1)$ of substantial local deformations (for β_c not too close to $\pi/2$), and both do not contain any adjustable parameters. For $\lambda Ca^{1/2} \geqslant \mathrm{O}(1)$, however, a new matching rule (4.22) is the one to use. The effect of $\tilde{h}_0$ on the results at $\tilde{h} \leqslant \mathrm{O}(1)$ vanishes, as $\tilde{h}_o \to \infty$ (we found $\tilde{h}_0 = 20Q_o$, where Q_o is the initial value of Q in (4.15), to suffice); an initial limitation $h_o \ll a_i$ is technically not important.

Thin-film equations are known to be very stiff, especially for the initial approach [22,36]. For $\tilde{\lambda} = 0$, a very efficient *absolutely stable*, semi-implicit matrix-iterative method was developed [22], which is, on average, $\mathrm{O}(N^2)$-intensive per time step (where N is the number of radial nodes). For limited use in the present work (Section 6), we have developed an $\mathrm{O}(N^3)$, but still quite efficient, absolutely stable algorithm for solving thin-film equations (4.11)–(4.15) at arbitrary $\tilde{\lambda}$, by generalizing the matrix part of the algorithm [22], as described below.

A semi-implicit scheme is used to make (4.11)–(4.15) linear with respect to $\tilde{h}$, $\tilde{u}$, $\tilde{f}$ and $\tilde{p}$ at a new time $\tilde{t}^{(\nu+1)}$, given the gap profile $\tilde{h}^{(\nu)}$ at the previous time $\tilde{t}^{(\nu)}$:

$$\tilde{r}\tilde{p}^{(v+1)} = -\frac{\partial}{\partial\tilde{r}}\left(\tilde{r}\frac{\partial\tilde{H}^{(v+1)}}{\partial\tilde{r}}\right), \tag{4.28}$$

$$\frac{2\tilde{f}^{(v+1)}}{\tilde{h}^{(v)}} = -\frac{\partial\tilde{p}^{(v+1)}}{\partial\tilde{r}}, \tag{4.29}$$

$$\tilde{u}^{(v+1)}(\tilde{r}) = \int_0^\infty \phi(\tilde{r}',\tilde{r})\tilde{f}^{(v+1)}(\tilde{r}')\,\mathrm{d}\tilde{r}', \tag{4.30}$$

$$\tilde{r}q + \frac{\partial}{\partial\tilde{r}}\left[\tilde{r}\tilde{h}^{(v)}\bar{u}\right] = 0, \quad \bar{u} = \tilde{u}^{(v+1)} - \frac{\tilde{\lambda}\left(\tilde{h}^{(v)}\right)^2}{12}\frac{\partial\tilde{p}^{(v+1)}}{\partial\tilde{r}}, \tag{4.31}$$

$$\int_0^\infty \tilde{p}^{(v+1)}\tilde{r}\,\mathrm{d}\tilde{r} = Q, \tag{4.32}$$

where

$$\tilde{H} = \tilde{h} - \frac{1}{2}\tilde{r}^2, \quad q = \frac{\tilde{h}^{(v+1)} - \tilde{h}^{(v)}}{\Delta t}, \tag{4.33}$$

and a second-order finite-difference discretization with respect to $\tilde{r}$ is used on a uniform mesh

$$0 = \tilde{r}_0 < \tilde{r}_1 < \cdots \tilde{r}_N = \tilde{r}_{\max}. \tag{4.34}$$

Using the trapezoidal rule and integrating the first equation (4.31) from $\tilde{r} = 0$ to $\tilde{r} = \tilde{r}_i$ gives an expression for $\bar{u}(\tilde{r}_i)$ in terms of $q(\tilde{\boldsymbol{r}}_j)$ $(0 \leqslant j \leqslant i)$; in the matrix form

$$\bar{\boldsymbol{u}} = \boldsymbol{A}_0 \cdot \boldsymbol{q} \tag{4.35}$$

with the bold letters denoting vectors of values at all mesh points 0, 1,…, N, and $\boldsymbol{A}_0$ being a triangular $(N+1)\times(N+1)$ matrix. On the other hand, using (4.29) and (4.30) and the second equation (4.31) yields

$$\frac{\tilde{\lambda}\tilde{h}^{(v)}(\tilde{r})}{6}\tilde{f}^{(v+1)}(\tilde{r}) + \int_0^\infty \phi(\tilde{r}',\tilde{r})\tilde{f}^{(v+1)}(\tilde{r}')\,\mathrm{d}\tilde{r}' = \bar{u}. \tag{4.36}$$

Discretizing the integral (4.36) like in [22], and substituting (4.35) into (4.36), we can consider (4.36) as a matrix equation for $\tilde{\boldsymbol{f}}^{(v+1)}$, which is solved by Gaussian elimination to give

$$\tilde{\boldsymbol{f}}^{(v+1)} = \boldsymbol{A}_1\boldsymbol{q}, \tag{4.37}$$

where $\boldsymbol{A}_1$ is a full $(N+1)\times(N+1)$ matrix. Eq. (4.37) parallels (4.8) of [22], although the procedure for calculating $\boldsymbol{A}_1$ is very different. In particular, in [22], the inverted form of the local boundary integral (4.13) was used

$$\tilde{f}(\tilde{r}) = 4\int_0^\infty \phi(\tilde{r}',\tilde{r})\left[\frac{1}{\tilde{r}'^2} - \frac{1}{\tilde{r}'}\frac{\partial}{\partial\tilde{r}'} - \frac{\partial^2}{\partial\tilde{r}'^2}\right]\tilde{u}(\tilde{r}')\,\mathrm{d}\tilde{r}', \tag{4.38}$$

which was advantageous at $\tilde{\lambda} = 0$ to greatly reduce the effect of the cutoff radius $\tilde{r}_{\max}$. In contrast, in the present problem with $\tilde{\lambda} = \mathrm{O}(1)$, the inverted form (4.38) has serious convergence difficulties at $\tilde{r} \to \infty$, and using (4.13) instead was found to be much better. Such a different behavior is due to the far-field asymptotics

$$\tilde{f}(\tilde{r}) = \mathrm{O}(\tilde{r}^{-3}), \quad \tilde{p}(\tilde{r}) = \mathrm{O}(\tilde{r}^{-4}), \tag{4.39}$$

in the present problem at $\tilde{\lambda} \neq 0$ (in contrast to $\tilde{f} \sim \tilde{r}^{-2}$ and $\tilde{p} \sim \tilde{r}^{-3}$ in [22]).

The next steps of the algorithm almost parallel (4.11)–(4.14) of [22], the difference being in using (4.39) instead of $\tilde{f} \sim \tilde{r}^{-2}$, $\tilde{p} \sim \tilde{r}^{-3}$. Namely, (4.29) is integrated from $\tilde{r}_{\max}$ to r_i, with the initial condition $\tilde{p}_N^{(\nu+1)} = \tilde{f}_N^{(\nu+1)}/\tilde{r}_N$ taken from (4.39), to express $\tilde{p}^{(\nu+1)} = \boldsymbol{A}_2 \cdot \boldsymbol{q}$, where $\boldsymbol{A}_2$ is another full $(N+1)\times(N+1)$ matrix. Substituting this expression into the normal stress balance (4.28) yields, by (4.33), a matrix equation for $\boldsymbol{q}$, solved by another Gaussian elimination, to within an arbitrary additive constant C in the film thickness. This constant is determined to satisfy the force balance (4.32); the tail of the integral (4.32) is approximated as $\frac{1}{2}\tilde{p}_N^{(\nu+1)}\tilde{r}_N^2$ using, again, (4.39). Knowing $\boldsymbol{q}$ allows us to proceed to the next time step, according to (4.33).This algorithm is *absolutely stable*, and so the time step is only limited by accuracy requirements. A more economical rule than that in [22] was used for the time step

$$\Delta\tilde{t} = c_{\Delta t} \min_i \frac{\tilde{h}_i}{\left|\partial\tilde{h}_i/\partial\tilde{t}\right|}, \tag{4.40}$$

where the minimum is taken over all mesh nodes $i = 0,1,\ldots,N$, and $c_{\Delta t} \ll 1$ is a numerical factor; values of $c_{\Delta t} \sim 0.01 - 0.03$ typically provide sufficiently small time integration errors (smaller $c_{\Delta t}$ would be needed in a special case $\beta_c \approx \pi/2$). The form (4.40) allows us to greatly increase Δt at a slow, quasi-stationary stage of film drainage, after the dimple forms. On the other hand, the form (4.40) refines the time step shortly before drop separation in 3D calculations. Finally, the algorithm features a variable value $\tilde{r}_{\max} = c_R\tilde{h}_{\min}^{1/2}$ of the cutoff radius, and mesh expansion/contraction [22], unless a dimple is present. The coefficient c_R is in the range $c_R \geqslant 25$ for $\tilde{\lambda} \geqslant O(1)$, to make the effect of the cutoff radius $\tilde{r}_{\max}$ negligible; at $\tilde{\lambda} = 0$, however, larger $c_R \sim 10^2$ were needed for numerical convergence in the separation zone. For uniform meshes, an elliptic type kernel $\phi(\tilde{r}', \tilde{r})$ need not be recalculated when the mesh expands or contracts, since $\phi(\tilde{r}', \tilde{r})$ depends on $\tilde{r}'/\tilde{r}$.

As a test, we ran this algorithm to $\tilde{t} = 2000$ for a constant driving force $Q \equiv 1$, $\tilde{h}_o = 4$, using $N = 200$ radial nodes, $c_R = 25$, $c_{\Delta t} = 0.024$ for $\tilde{\lambda} = 20$ and $c_{\Delta t} = 0.048$ for $\tilde{\lambda} = 2$; the results for the minimum film thickness $\tilde{h}_{\min}(\tilde{t})$ were unaffected in the entire range $0 \leqslant \tilde{t} \leqslant 2000$ by increasing N up to 400, c_R up to 40, and decreasing $c_{\Delta t}$ to 0.006. These simulations took only about 200 and 400 time steps from $\tilde{t} = 0$ to $\tilde{t} = 2000$ (14 and 29 s) for $\tilde{\lambda} = 2$ and 20, respectively. For comparison, the explicit method requires at least $O(10^6)$ $O(N^2)$-intensive time steps for each of these simulations. The LHS of (4.36) is a positive-definite operator making conjugate gradient iterative solution of (4.36) quite efficient compared to Gaussian elimination; accordingly, the techniques of approximate factorizations [22] could be used, to make the present method, on average, $O(N^2)$-intensive per time step. It appears, however, that, even in the $O(N^3)$ version, the present approach is much less expensive to apply systematically than explicit techniques. With van der Waals forces included, our algorithm can be used in future work to extend systematic coalescence efficiency calculations [22,23] to high λ, where the thin-film equations (4.11)–(4.15) would need to be solved many thousand times.

5. Validation and efficiency of the algorithm

5.1. Gravity-induced motion

In the numerical results below for two drops of non-deformed radii a_1, a_2 ($a_1 < a_2$) settling under gravity, the characteristic time scale is $8\pi\mu_e/(|\Delta\rho|ga_2)$, for consistency with our earlier work [29]. The drops start far apart from spherical shapes, with initial horizontal Δx_o and vertical Δz_o center-to-center offsets. Fig. 9 presents snapshots of the simulation for matching viscosities, $Ca = \mu_e|\boldsymbol{V}_1^\infty - \boldsymbol{V}_2^\infty|/\sigma \approx 0.036$, and moderately adaptive surface discretizations with $N_\triangle = 35K$ triangles per drop (below, abbreviations 35K, 138K, etc.

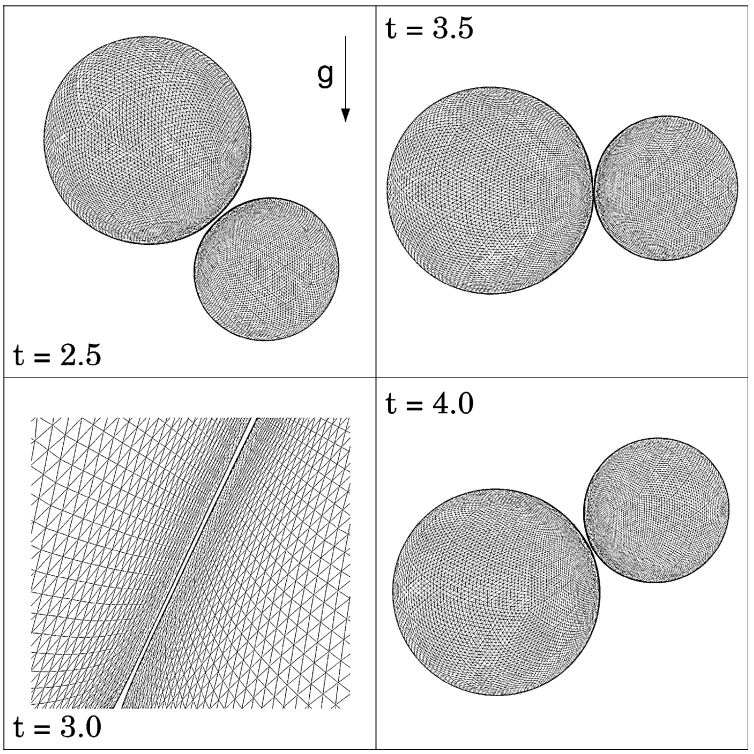

Fig. 9. Relative gravity-induced motion simulation with $a_1/a_2 = 0.7$, $\lambda = 1$, $Ca = 0.036125$, $\Delta x_o = 0.5a_2$, $\Delta z_o = 5.0874a_2$, $N_\triangle = 35\text{K}$ ($M_\triangle = 180$), $k_0 = 20$, $L = 2$ (MA1), $K_{\Delta t} = 3.5$, $\varepsilon = 10^{-8}$. The drops sediment downwards. A close-up at $t = 3$ shows the gap of $1.64 \times 10^{-3} a_2$.

stand for an exact number of triangular elements 34560, 138240, etc. used); only the near-contact stage of relative motion is shown. The surface clearance $h_{\min}$ was calculated, like in [29], as the minimum of node-to-node, node-to-face, node-to-edge, and edge-to-edge distances between two flat drop triangulations. Spherical drops would touch at the collision angle $\beta_c = 0.851$ rad. Due to deformation, however, the drops remain separated, with $h_{\min}$ reaching $7.2 \times 10^{-4} a_2$ at $t = 3.79$ ($\beta = 1.85$ rad), and eventually depart. A close-up at $t = 3$ ($\beta = 1.12$ rad) shows the gap of $h_{\min} \sim 10^{-3} a_2$, and well-controlled gap-adaptive meshes. For the snapshots in Fig. 9, the ratio $r_{\max}/r_{\min}$ of the maximum mesh edge (in the outer region) to the minimum mesh edge (in the gap) is in the range 5–8. The multipole-accelerated boundary-integral calculations in (3.2) (i.e., one half of one time step) took 9.9–11.8 s for each $2.5 \leqslant t \leqslant 4$. The calculations are even faster for well-separated drops (e.g., 7.8 s for $t = 2$, when $h_{\min} = 0.21a_2$). These times may be compared to 75.4 s required for the standard, non-multipole point-to-point calculations in (3.2). The whole near-contact stage of the simulation took about 13,000 second-order Runge–Kutta steps (about 80 h of CPU time).

To verify convergence of our code to the standard, point-to-point summation algorithm, the run in Fig. 9 was interrupted at $t = 3.5$ (when $h_{\min} = 0.0011a_2$) to compare our normal fluid velocities $q_i = \boldsymbol{u}(\boldsymbol{x}_i) \cdot \boldsymbol{n}(\boldsymbol{x}_i)$ with exact values q_i^{ex} (for a given triangulation) obtained by the standard method. Two criteria were used to quantify deviation between q and q^{ex}:

$$\delta_1(q, q^{\text{ex}}) = \frac{1}{\langle |q^{\text{ex}}| \rangle} \max_{\boldsymbol{x}_i \in S_1, S_2} \left| q_i - q_i^{\text{ex}} \right|, \quad \delta_2(q, q^{\text{ex}}) = \langle |q - q_{\text{ex}}| \rangle / \langle |q_{\text{ex}}| \rangle, \tag{5.1}$$

Table 1
The convergence of the present solution q to the standard $O(N_\triangle^2)$ solution q^{ex} as $\varepsilon \to 0$, for gravity-induced motion ($\lambda = 1$, $k_0 = 20$)

	$N_\triangle = 35K$, $M_\triangle = 180$			$N_\triangle = 138K$, $M_\triangle = 320$		
ε	δ_1	δ_2	CPU time (s)	δ_1	δ_2	CPU time (s)
10^{-5}	2.5×10^{-3}	4.0×10^{-5}	6.0	7.7×10^{-3}	2.3×10^{-5}	18.4
10^{-6}	5.7×10^{-4}	5.7×10^{-6}	7.3	5.2×10^{-4}	4.2×10^{-6}	21.5
10^{-7}	1.5×10^{-4}	6.9×10^{-7}	8.9	7.6×10^{-5}	6.4×10^{-7}	25.0
10^{-8}	2.1×10^{-5}	9.4×10^{-8}	10.9	5.8×10^{-6}	8.6×10^{-8}	29.2
10^{-9}	3.3×10^{-6}	1.2×10^{-8}	13.4	7.6×10^{-7}	1.0×10^{-8}	34.8

where $\langle\cdots\rangle$ denotes averaging over both surfaces. Table 1 demonstrates that $\delta_1, \delta_2 \to 0$ as $\varepsilon \to 0$, confirming the convergence, and CPU times grow only slightly with tightening the "precision parameter" ε. For $\varepsilon = 10^{-8}$ used in the dynamical simulation of Fig. 9, multipole truncation does not affect the normal velocities, on the average, to 7 digits.

In multidrop simulations with moderate triangulations [8,10,11] we observed larger effects of multipole acceleration, even for a similar total number of mesh nodes (e.g., for $N = 64$ drops with $N_\triangle = 1280$ triangles per drop, the gain over standard summations was 35–47 times, depending on the precision parameter). There are several factors, all acting to make a free-space configuration of two nearly touching drops somewhat less favorable for multipole acceleration than a multidrop configuration with periodic boundaries and $N_\triangle \sim 10^3$ triangles per drop. First, a far-field part, associated with periodic images, which is costly to calculate in a point-to-point manner, is absent in the present problem. Second, a large number of nodes in the gap region, especially for gap-adaptive meshes, leads to substantial overlapping of spherical shells $\mathscr{D}_\gamma$ around patches, thereby increasing the weight of direct summations in the present algorithm. Next, singularity and near-singularity subtractions, which are relatively inexpensive to calculate in the multidrop codes due to modest $N_\triangle \sim 10^3$, considerably contribute to the cost of the present algorithm. Finally, unlike multidrop simulations at finite deformation, the present runs necessarily require tight precisions $\varepsilon \leqslant O(10^{-7}\text{–}10^{-8})$, since we are interested in accurately tracking surface separations $h_{\min}/a_i$ of order 10^{-3}–10^{-4}. Nevertheless, the observed 7- to 10-fold gains over the standard method are still significant. Note also that the present simulations require a very large total number of time steps, due to numerical stiffness at small deformations, making runs necessarily expensive and multipole acceleration very helpful; this acceleration is even more indispensable for contrast viscosities (see below).

To further test our algorithm, the simulation in Fig. 9 was repeated with $\varepsilon = 10^{-8}$ and non-adaptive ($L = 0$) very high triangulations $N_\triangle = 138K$. Again, at $t = 3.5$, convergence to the results by the standard summation method (requiring 21 min of CPU time) is observed, as $\varepsilon \to 0$ (Table 1); for $\varepsilon = 10^{-8}$, the gain over the standard method is now 43-fold.

5.2. Shear-induced motion

In shear-induced motion simulations for two equal drops ($a_1 = a_2 = a$) in the plane of shear $\theta = \pi/2$, we used the special symmetric version (Section 3.2) of our multipole-accelerated code, which yields about two-fold gain over the general version for unequal drops. The drops started from spherical shapes, with initial center-to-center offsets Δy_o (across the flow) and Δx_o (along the flow). Fig. 10 presents snapshots of relative motion for $\lambda = 1$, $Ca = \mu_e \gamma a/\sigma = 0.01$, and moderately adaptive discretizations with $N_\triangle = 35K$ triangles per drop; time is scaled with γ^{-1}. These snapshots show how small the global deformation is, and the surface clearances of $h_{\min} = 3.2\times10^{-3}a$ and $7.3\times10^{-4}a$ for $t = 5.5$ and 6.5, respectively, due to deformation. The simulation was repeated for $N_\triangle = 78K$ and 138K to study the triangulation effects (see below). Additionally, to check the correctness and performance of the symmetric version of our code for $\lambda = 1$, the run with

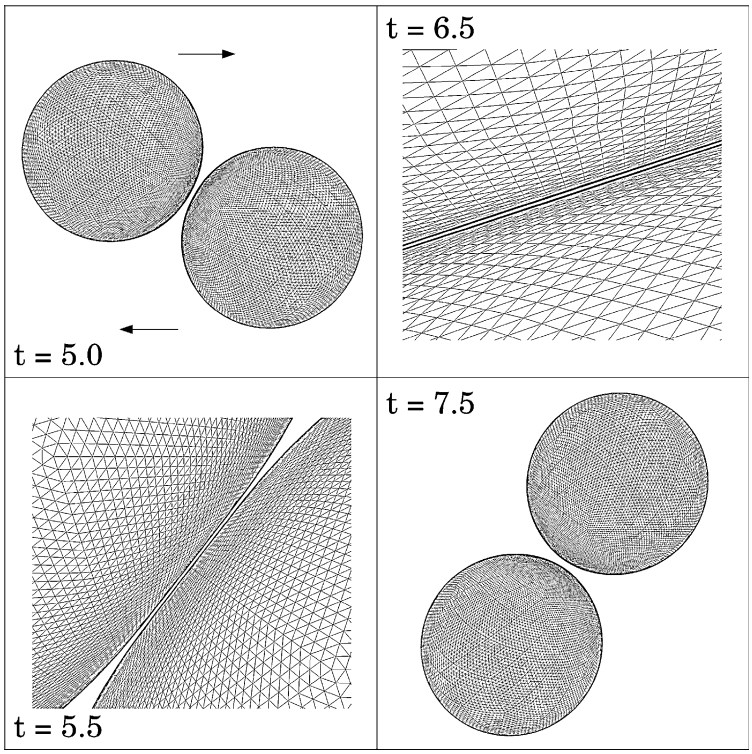

Fig. 10. Relative shear-induced motion of two equal drops in the plane of shear for $\lambda = 1$, $Ca = 0.01$, $\Delta x_o = 5a$, $\Delta y_o = 0.7a$, $N_\triangle = 35$K ($M_\triangle = 180$), $L = 2$ (MA1), $K_{\Delta t} = 3.5$, $\varepsilon = 10^{-8}$. Close-ups at $t = 5.5$ and 6.5 show the gaps of $3.2 \times 10^{-3}a$ and $7.3 \times 10^{-4}a$, respectively.

$N_\triangle = 78$K was interrupted at $t = 7$ ($h_{\min} = 9.3 \times 10^{-4}a$), to verify convergence to the results by the standard point-to-point summation technique for the same configuration; again, δ_1, $\delta_2 \to 0$, as $\varepsilon \to 0$ (Table 2). At $t = 7$ and $\varepsilon = 10^{-8}$, one half of the time step takes 14.2 s by our code (compared to about 100 s for the best direct summation algorithm); for separated drops, it is even faster (8–10 s). The near-contact stage (t from 5.25 ($h_{\min} = 0.01a$) to separation $t = 7.28$) took about 28,000 second-order RK steps (9 days of CPU time by our code) for $N_\triangle = 78$K; again, direct summations would be very expensive to run dynamically in this and similar simulations.

A natural question is whether accurate results could be achieved with much smaller triangulations (like a few thousand elements per drop) but much stronger mesh adaptation in the gap. Fig. 11 shows the non-dimensional surface clearance, $h_{\min}/a$, vs. β-angle for three different triangulations. The long-dashed line

Table 2
The convergence of the present solution to the standard $O(N_\triangle^2)$ solution for shear-induced motion ($N_\triangle = 78$K, $M_\triangle = 240$, $k_o = 23$, $L = 3$, MA3, $\lambda = 1$)

ε	δ_1	δ_2	CPU time (s)
10^{-5}	1.7×10^{-3}	1.7×10^{-5}	9.3
10^{-6}	1.4×10^{-4}	2.2×10^{-6}	10.5
10^{-7}	1.6×10^{-5}	2.5×10^{-7}	12.3
10^{-8}	1.5×10^{-6}	3.0×10^{-8}	14.2
10^{-9}	8.3×10^{-8}	3.9×10^{-9}	17.0

β-angle for shear-induced motion with

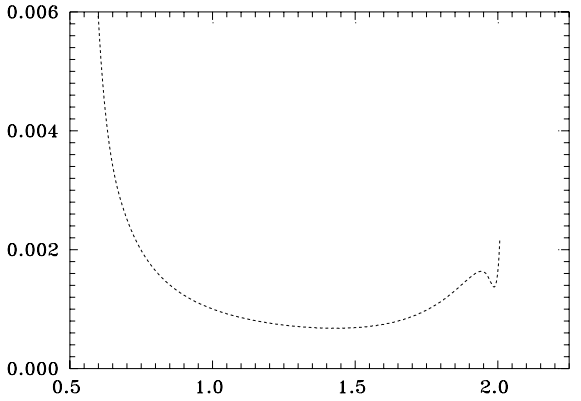

Fig. 11. Non-dimensional surface clearance vs.

is for a strongly adaptive mesh with $N_\triangle = 12$K, the mesh edge ratio r_{max}/r_{min} being about 21 during near-contact. The gap resolution for $N_\triangle = 12$K is about the same as for $N_\triangle = 78$K, but $h_{min}(\beta)$ for $N_\triangle = 12$K fails to be accurate due to the lack of *outer* resolution (which is much worse than for $N_\triangle = 78$K), while the results for $N_\triangle = 78$K converge very well. Despite a seeming simplicity of the outer region (nearly spherical shapes), it must be represented in the boundary-integral method for $Ca \ll 1$ with very high accuracy, since, in the non-dimensional form of the single-layer potential (2.4) and (2.5), a small curvature deviation from a uniform value is divided by Ca to produce an O(1)-effect. Likewise, numerical errors in the integration (2.4) are amplified by a factor of Ca^{-1}. Additionally, a strong mesh non-uniformity inherent in small, overadaptive triangulations affects adversely the curvature calculation and the global accuracy of surface integration. For convergent boundary-integral calculations of this kind, *both* inner and outer resolutions must be greatly increased and without bound, as $Ca \to 0$. For each $Ca \ll 1$, there is an optimum degree of mesh adaptivity that we did not try to determine; it is less important for the present multipole-accelerated algorithm, since a decrease in mesh adaptivity is counterbalanced by faster performance per time step for a more uniform mesh at the same $N_\triangle$.

Due to smoothness of the outer region, it might be tempting to use high-order numerical approximations to reduce the required number of boundary elements; our experience, however, has been negative. For example, the run with $N_\triangle = 12$K was repeated using local fourth-order approximation of the shape function $R(x, y)$ instead of quadratic fitting (3.19), as described in Section 3.3, which gives, generically, high order of accuracy for curvatures and normals. The results (symbols in Fig. 11) show, indeed, a great accuracy improvement for $h_{min}(\beta)$ at the initial stage of approach, but no improvement at all during near-contact motion of most interest. It appears that high-order approximations are not advantageous in this problem at $Ca \to 0$, and large triangulations cannot be avoided, regardless of the method.

Turning to the case of drops with arbitrary viscosity, Fig. 12 presents snapshots of relative motion for $\lambda = 10$, $Ca = 0.005$, and moderately adaptive triangulations with $N_\triangle = 46$K. The mesh edge ratio r_{max}/r_{min} is about 11 for most of near-contact motion (and about 8.5 at separation $t = 9.14$). The iterations of the boundary-integral equation (2.7) were terminated once the residual in all mesh nodes was less than 10^{-4} of the average variation of $\boldsymbol{w}$ on S_α (similar to the criterion (2.10) in [8]); typically 4–7 iterations during most of the near-contact motion, and about 10 iterations close to separation sufficed (well-separated configurations required one iteration). The gaps for near-contact are almost an order of magnitude larger than for the same Ca and $\lambda = 1$ (see Fig. 17) due to much stronger film resistance at $\lambda \gg 1$. Nevertheless, mesh-independent calculations for $\lambda = 10$ are almost as difficult, because the double-layer integral (2.7), essential for $\lambda = 10$, is much more sensitive to discretization errors than is the single-layer integral (2.4), other conditions

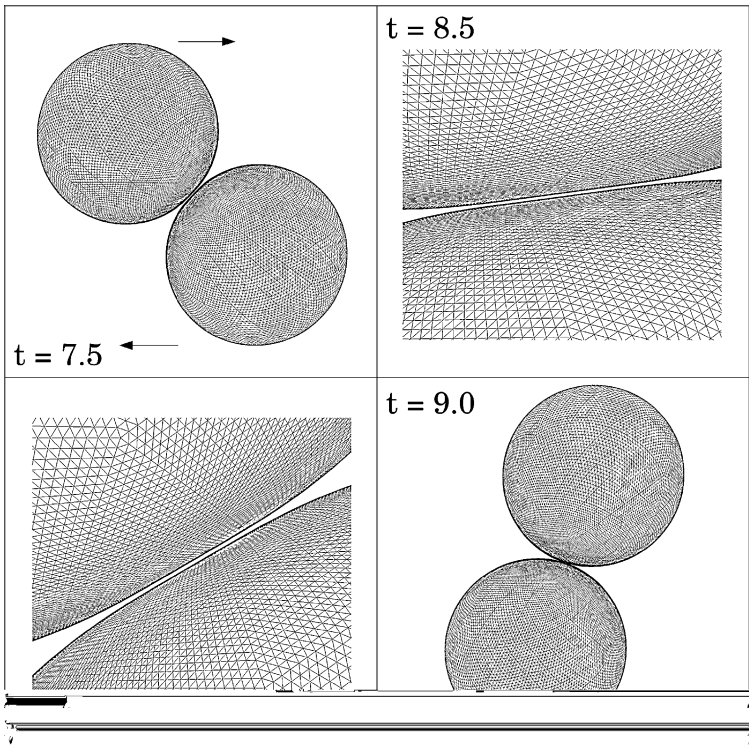

Fig. 12. Relative shear-induced motion of two equal drops in the plane of shear for $\lambda = 10$, $Ca = 0.005$, $\Delta x_o = 5a$, $\Delta y_o = 0.5a$, $N_\triangle = 46\text{K}$ ($M_\triangle = 240$), $L = 4$ (MA2), $K_{\Delta l} = 7$, $\varepsilon = 3 \times 10^{-7}$. Close-ups at $t = 8$ and 8.5 show the gaps of $4.5 \times 10^{-3}a$ and $2.8 \times 10^{-3}a$, respectively, and a well-controlled mesh.

being equal. Again, due to a large size of our code, it was crucial to validate the double-layer part by comparing with the standard point-to-point summation algorithm. The run in Fig. 12 was repeated for $N_\triangle = 82\text{K}$ and interrupted at $t = 8.53$ ($\beta = 1.97$ rad) to calculate the deviations (5.1) of the normal velocities (after one iteration, for simplicity) from those obtained by the standard method for the same configuration. Table 3 demonstrates the necessary convergence $\delta_1, \delta_2 \to 0$, as the precision parameter ε is tightened. The CPU times per iteration are also shown in Table 3; in part, such a performance at $N_\triangle = 82\text{K}$ in near contact is achieved by precalculating the subtraction tensor (3.5) (at the expense equivalent to about two extra iterations). For $\varepsilon = 3 \times 10^{-7}$ used in the dynamical simulation and $t = 8.53$, an almost 19-fold gain in the iter-

Table 3
The convergence of the present solution to the standard $O(N_\triangle^2)$ solution for shear-induced motion in the double-layer test ($N_\triangle = 82\text{K}$, $M_\triangle = 320$, $k_o = 22$, $\lambda = 10$)

ε	δ_1	δ_2	CPU time (s) per iteration
3×10^{-5}	5.0×10^{-4}	1.3×10^{-5}	7.7
3×10^{-6}	3.3×10^{-5}	1.9×10^{-6}	9.4
3×10^{-7}	3.8×10^{-6}	3.6×10^{-7}	11.4
3×10^{-8}	5.8×10^{-7}	5.1×10^{-8}	14.2
3×10^{-9}	6.0×10^{-8}	4.1×10^{-9}	17.3

ation speed is observed over the standard method. For $N_{\triangle} = 82$K, the whole near-contact motion ($7.4 \leqslant t \leqslant 9.4$) took about 23000 second-order RK steps.

6. Comparisons with asymptotic theories

6.1. Gravity-induced motion

In Fig. 13(a) and (b), the non-dimensional surface clearance, $h_{\min}/a_2$, is shown vs. β-angle for $\lambda = 1$ and two capillary numbers; the results for different triangulations show very good convergence. For $Ca \approx 0.14$ (Fig. 13(a)), the minimum clearance is not too small ($h_{\min}/a_2 \geqslant 8.3 \times 10^{-3}$), and there is an appreciable global deformation similar to that in Fig. 11 of [29] for a different offset of $\Delta x_o = 0.325a_2$. At this relatively large Ca, the asymptotic theory [22] is not accurate, underpredicting $h_{\min}$. For a more challenging case $Ca \approx 0.036$ (Fig. 13(b)), we were still able to accurately trace the surface clearance $h_{\min}$ to $7.4 \times 10^{-4}a_2$. At this smaller Ca, the asymptotic theory becomes acceptable.

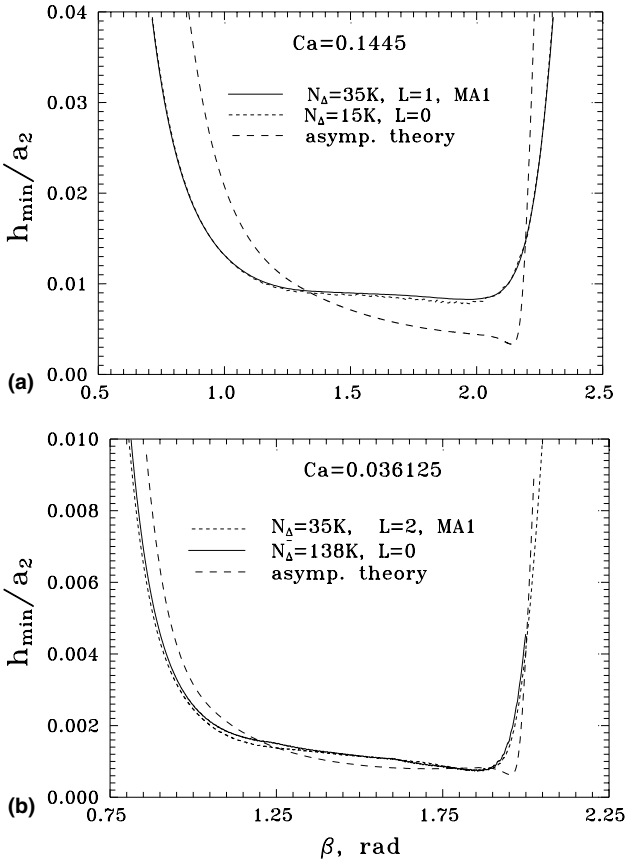

Fig. 13. Non-dimensional surface clearance vs. β-angle (β increases as time proceeds) for gravity-induced motion with $a_1/a_2 = 0.7$, $\lambda = 1$, $\Delta x_0 = 0.5a_2$, $\Delta z_0 = 5.0874a_2$. —— and - - - - -, boundary integral; – – –, $\tilde{\lambda} = 0$ asymptotic theory (with $\alpha = 6.423$, $T = 0.2913$, $\beta_c = 0.8511$).

From Fig. 13(a) and (b), it is natural to define the "separation angle" β_{sep} as the value of β corresponding to the last local minimum of $h_{min}(\beta)$ (in general, there are more than one minima, see Fig. 11); as β exceeds β_{sep}, h_{min} starts to increase sharply (especially at smallest Ca), and the drops eventually separate. Intuitively, one could predict $\beta_{sep} \to \pi/2$ at $Ca \to 0$, since $\pi/2$ is the value of β with the vanishing contact force (4.2). At first glance, it is surprising from Fig. 13(a) and (b) that β_{sep} decreases only slightly and remains considerably higher than $\pi/2$, when Ca is decreased from 0.14 to 0.036. Since the asymptotic calculations adequately predict the separation angle for $Ca = 0.036$ (Fig. 13(b)), we continued them to much smaller Ca to evaluate the asymptotics of β_{sep} at $Ca \to 0$. Fig. 14 shows that $(\beta_{sep} - \pi/2)/Ca^{1/3} = O(1)$, as $Ca \to 0$.

Remarkably, this extremely slow approach $\beta_{sep} = \frac{\pi}{2} + O(Ca^{1/3})$ is also a consequence of rescaling properties of the thin-film equations (4.11)–(4.15) and (4.18) for $\tilde{\lambda} = 0$ in the vicinity of $\beta = \pi/2$ (Appendix C). The same rescaling analysis shows that the minimum surface separation along the trajectory, $\min(h_{min}/a_2)$, scales like $Ca^{4/3}$. Our asymptotic thin-film calculations fully support this theoretical scaling : indeed,

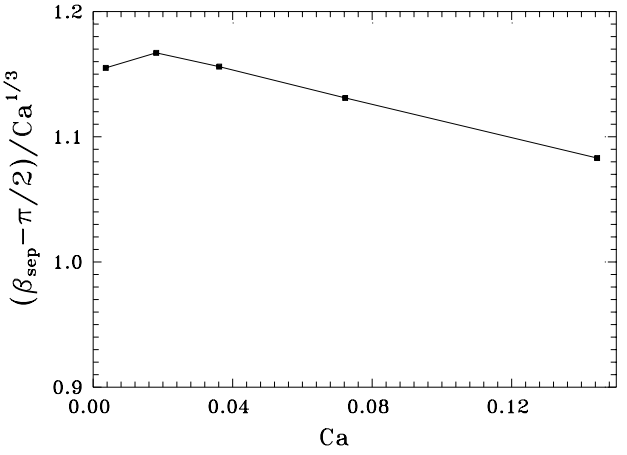

Fig. 14. Deviation of the separation angle β_{sep} from $\pi/2$, scaled with $Ca^{1/3}$ in the $\tilde{\lambda} = 0$ asymptotic calculations for gravity-induced motion.

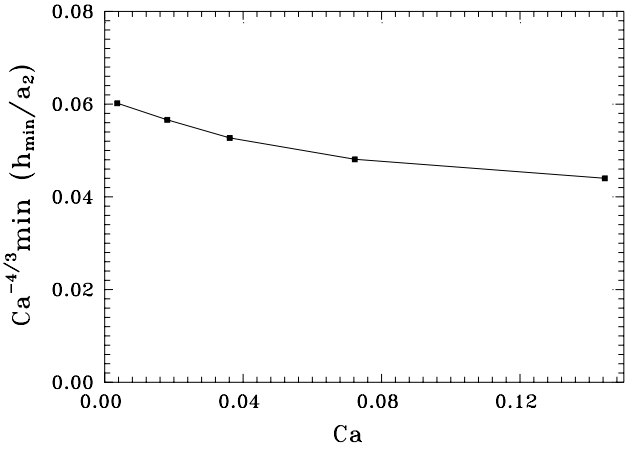

Fig. 15. Minimum surface clearance along a trajectory scaled with $Ca^{4/3}$, in the $\tilde{\lambda} = 0$ asymptotic calculations for gravity-induced motion.

$Ca^{-4/3}\min(h_{\min}/a_2)$ remains O(1), as $Ca \to 0$ (Fig. 15). Note that $Ca^{4/3}$ is the ultimate scaling for $\min(h_{\min}/a_2)$; at moderately small Ca, exact calculations (Fig. 13(a) and (b)) show a faster decay: for Ca varying from 0.14 to 0.036, $\min h_{\min}$ decreases about 11 times. This strong dependence of $h_{\min}$ on Ca, together with film localization, are among the reasons that make convergent boundary-integral calculations very difficult when Ca is reduced.

6.2. Shear-induced motion

In Fig. 16(a) and (b) for $\lambda = 1$ and two different capillary numbers, the solid lines are from fully convergent boundary integral (BI) calculations. The short-dashed and long-dashed lines are from the asymptotic theory [22,23] (hereafter referred to as the "$\tilde{\lambda} = 0$ theory") and from the asymptotic theory of Section 4 for highly viscous drops (referred to as the "$\tilde{\lambda} \neq 0$ theory"), respectively. In both cases $Ca = 0.04$ (Fig. 16(a)) and $Ca = 0.01$ (Fig. 16(b)), the $\tilde{\lambda} = 0$ theory is noticeably closer to the exact results and preferred in this case of matching viscosities; for $Ca \to 0$, though, the two theories would coincide. Although the capillary numbers (2.8) and (2.9) for gravity-induced and shear-induced motion are defined differently, and cannot be

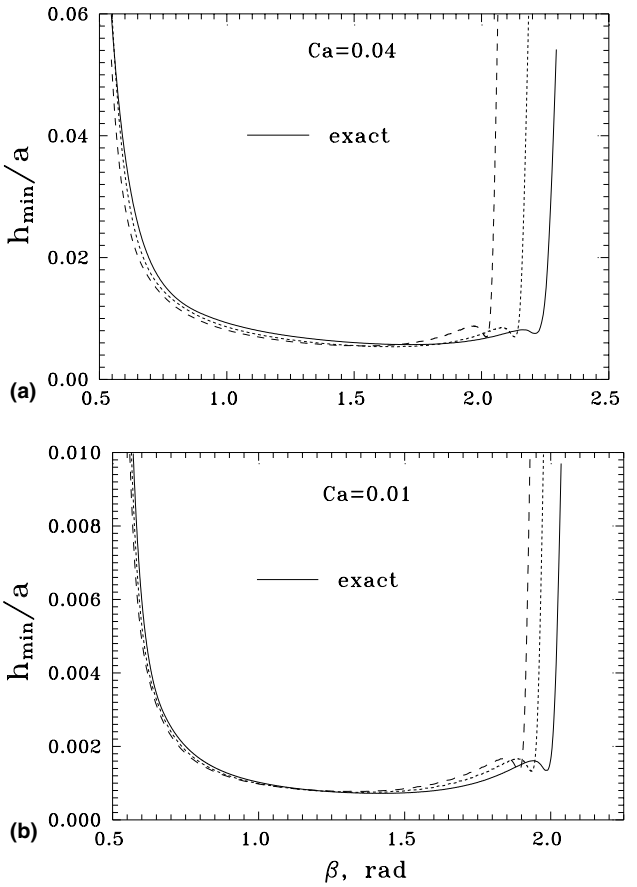

Fig. 16. Comparison of exact results with the $\tilde{\lambda} = 0$ (- - - -) and $\tilde{\lambda} \neq 0$ (– –) asymptotic theories for shear-induced motion at $\lambda = 1$, $\Delta x_0 = 5a$, $\Delta y_0 = 0.7a$. The parameters of the asymptotic theories are $D^* = 1.450$, $B' = 0.0685$, $\beta_c = 0.5468$ rad. In BI calculations (solid lines), full numerical convergence was reached with $N_\triangle = 35$K, $L = 1$, MA1 for $Ca = 0.04$, and $N_\triangle = 138$K, $L = 3$, MA3 for $Ca = 0.01$.

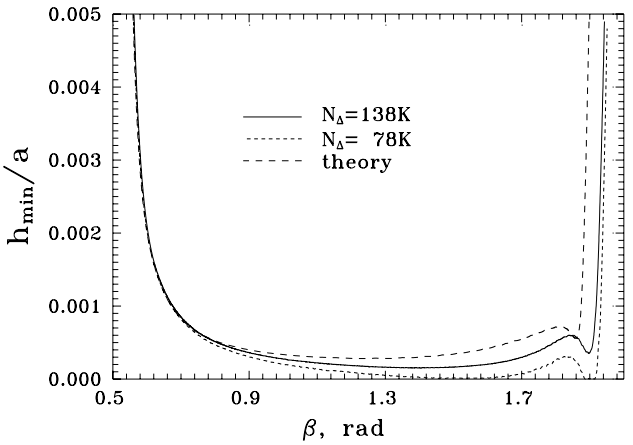

Fig. 17. Non-dimensional surface clearance vs. β-angle for shear-induced motion with $\lambda = 1$ and $Ca = 0.005$. —— and - - - - -, boundary integral (with $L = 2$, MA1); – – –, $\tilde{\lambda} = 0$ asymptotic theory.

compared directly to each other, some qualitative differences from the gravity-induced motion are observed in Fig. 16. While, for gravity-induced motion, the $\tilde{\lambda} = 0$ theory overpredicted the separation angle β_{sep} and had a limited accuracy for the entire curve $h_{min}(\beta)$ in the studied range of Ca (Fig. 13(a) and (b)), the situation is different for shear flow: the $\tilde{\lambda} = 0$ theory is very successful for $h_{min}(\beta)$ in the whole range, except for close to separation, where it slightly underestimates the separation angle compared to the exact result.

To further check the validity of this theory in describing the separation angle β_{sep}, we have attemped a much harder case $Ca = 0.005$ (Fig. 17). The two simulations with $N_\triangle = 78$K and 138K show excellent convergence up to $\beta = 0.7$ rad (when $h_{min}/a = 8.5 \times 10^{-4}$), but considerable deviation for larger β (solid and short-dashed lines). The $\tilde{\lambda} = 0$ asymptotic theory (long-dashed line) predicts the minimum clearance of $h_{min}/a = 2.81 \times 10^{-4}$ along the trajectory, indicative of how difficult convergent boundary-integral calculations must be in this case. Although we do not have exact results for $h_{min}(\beta)$ in the entire range at $Ca = 0.005$, the boundary-integral calculations in Fig. 17 demonstrate excellent numerical convergence for the separation angle β_{sep}, which is, therefore, less sensitive to triangulation error than is h_{min}. The calculation of β_{sep} is still non-trivial for this $Ca = 0.005$; a non-adaptive mesh with as many as 138K elements per drop (which failed to resolve h_{min} completely, but did simulate separation) gave $\beta_{sep} = 2.17$ rad, away from the correct result $\beta_{sep} = 1.88-1.89$ rad.

Fig. 18 presents a comparison between the exact and asymptotic ($\tilde{\lambda} = 0$ theory) values of the separation angle β_{sep}; as Ca varies from 0.04 to 0.005, the absolute error of the asymptotic theory decreases from 0.085 rad to about 0.022 rad. This modest, but noticeable discrepancy in the separation angle is likely due to the "pumping flow" (neglected in the leading-order asymptotic theory we are using) that drives the fluid away from the gap (at the tensile stage), thus delaying separation compared to the asymptotic result. There are current efforts to incorporate pumping flow effects in the thin-film equations [25], which may lead to future higher-order asymptotic algorithms valid in a wider range of capillary numbers. Our thin-film calculations in Fig. 18 for $Ca \to 0$ confirm the behavior $\beta_{sep} = \pi/2 + O(Ca^{1/3})$, in accordance with the rescaling in Appendix C. The same thin-film calculations reveal that, as $Ca \to 0$, the minimum separation along the trajectory, $\min h_{min}(\beta)$, is achieved in these examples at $\beta \approx 0.92$ rad (i.e., away from $\pi/2$) and has the same scaling $\sim aCa^{4/3}$, as the second (local) minimum of $h_{min}(\beta)$ at the separation point (Fig. 19). Thus, as the minimum gap is reached, it remains on the same order $\sim aCa^{4/3}$ until drops separate (note this result is obtained for finite offsets $\Delta y_o \sim a$, and is not necessarily true for collisions close to head-on). Interestingly, other authors [1] used qualitative arguments instead of detailed thin-film solutions to obtain the $aCa^{3/2}$-scaling for the

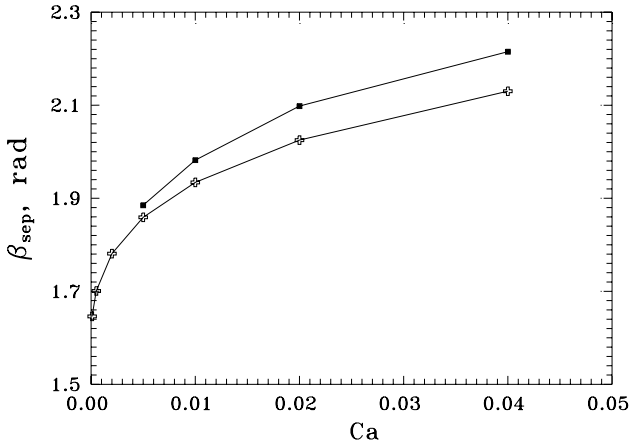

Fig. 18. Comparison between the exact (squares) and asymptotic (crosses, $\tilde{\lambda} = 0$ theory) values of the separation angle in shear-induced motion for $\lambda = 1$, $\Delta x_0 = 5a$, $\Delta y_0 = 0.7a$.

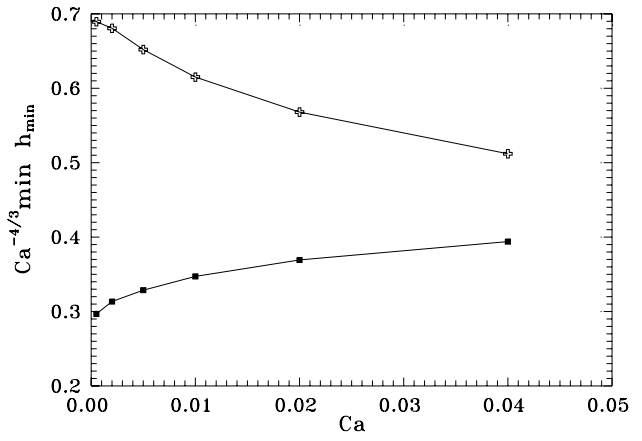

Fig. 19. The first (squares) and second (crosses) minima of $h_{\min}(\beta)$ scaled with $Ca^{4/3}$, from $\tilde{\lambda} = 0$ theory for shear-induced motion ($\lambda = 1$).

minimum gap, fairly close to our rigorous result $aCa^{4/3}$. The scaling $h_{\min}/a \sim Ca^{4/3}$ for the entire near-contact motion between the minima of $h_{\min}(\beta)$ also supports universality arguments used in Appendix C to derive the asymptotics of the separation angle.

While, for $\lambda = 1$, the $\tilde{\lambda} = 0$ theory is preferred, the situation is different for highly viscous drops. Fig. 20 presents the non-dimensional surface separation for $\lambda = 4$ and $Ca = 0.01$. Fully convergent BI results (solid line) are much closer to the predictions of the $\tilde{\lambda} \neq 0$ theory (long-dashed line) than to the results by the $\tilde{\lambda} = 0$ theory (short-dashed line). Both theories, however, give comparable errors (but of different signs) for the separation angle β_{sep}, which slowly disappear as $Ca \to 0$. For $Ca = 0.005$ (Fig. 21), convergence difficulties precluded us from accurate calculation of $h_{\min}(\beta)$ in the entire range, the difference between the results for $N_{\triangle} = 46$K and 82K reaching 30% at separation; a convergent value of $\beta_{\text{sep}} = 2.06$, however, was still achieved, close to the prediction 2.03 by the by the $\tilde{\lambda} \neq 0$ theory.

Similar calculations for $\lambda = 10$ and $Ca = 0.02$, 0.01 (Fig. 22(a) and (b)) confirm that the $\tilde{\lambda} \neq 0$ asymptotic theory becomes accurate for $h_{\min}$ at $Ca \leqslant 0.01$, and gives only a modest error for the separation angle (the

for obvious reasons). Again, at $Ca = 0.005$ (Fig. 23), our BI
se to separation, the difference between the results for
lowever, an accurate result for β_{sep} was still obtained, only
= 10, the $\tilde{\lambda} \neq 0$ asymptotic theory describes the separation
$= 0$ theory at $\lambda = 1$ (cf. Figs. 17 and 23). The behavior of
the naive expectation $\beta_{sep} \approx \pi/2$ than for $\lambda = 1$: β_{sep} varies
to 0.005. To observe $\beta_{sep} \to \pi/2$, much smaller Ca would
ndix C do not hold for $\tilde{\lambda} \neq 0$, and so the asymptotics
∞). It was predicted qualitatively [1] that the minimum
ops can reach along a trajectory scales like Ca, as
$Ca \leqslant 0.04$ closely follow this scaling.

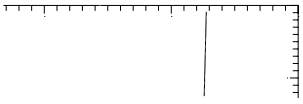

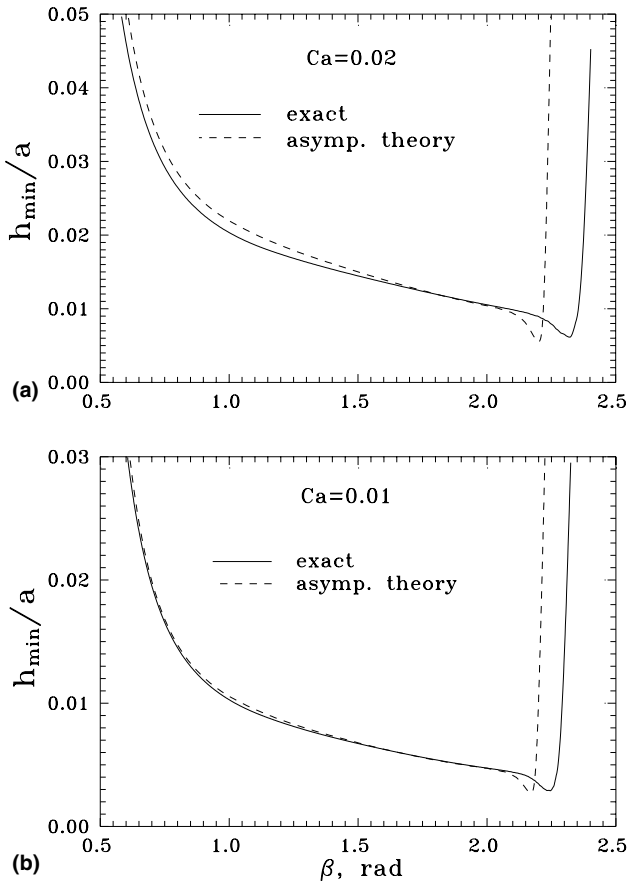

Fig. 22. Comparison of exact results with $\tilde{\lambda} \neq 0$ asymptotic theory for shear-induced motion at $\lambda = 10$, $\Delta x_0 = 5a$, $\Delta y_0 = 0.5a$. The theory parameters are $D^* = 1.870$, $B' = 0.1843$, $\beta_c = 0.7681$ rad. In BI calculations (solid lines), full numerical convergence was reached with $N_\triangle = 15$K, $L = 3$, MA2 for $Ca = 0.02$, and $N_\triangle = 46$K, $L = 4$, MA3 for $Ca = 0.01$.

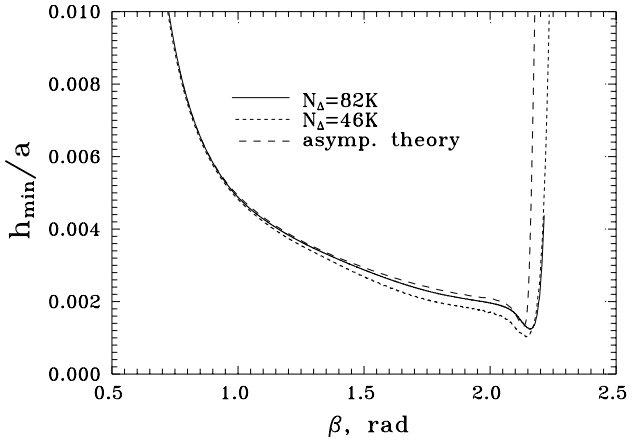

Fig. 23. Non-dimensional surface clearance vs. β-angle for shear-induced motion with $\lambda = 10$ and $Ca = 0.005$. —— and - - - - -, boundary integral (with $L = 4$, MA2); – – –, $\tilde{\lambda} \neq 0$ asymptotic theory.

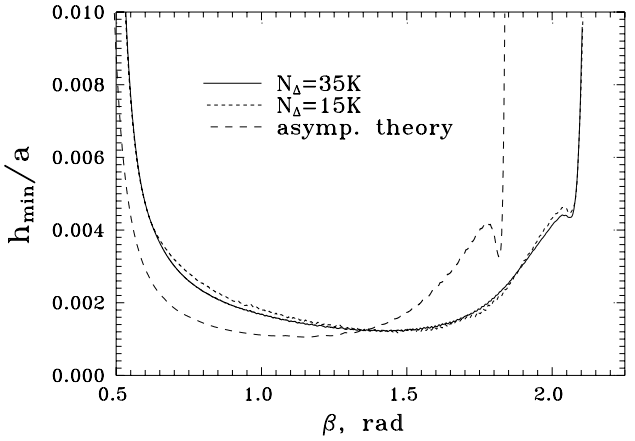

Fig. 24. Non-dimensional surface clearance vs. β-angle for shear-induced motion with $\lambda = 0.25$, $Ca = 0.04$, $\Delta y_o = 0.7a$, and $\Delta x_o = 5a$. —— and - - - - -, boundary integral (with $L = 4$, MA2); – – –, $\tilde{\lambda} = 0$ asymptotic theory (with $D^* = 1.227$, $B' = 0.0237$, $\beta_c = 0.4552$).

Similar calculations are far more expensive for $\lambda \ll 1$, and we have made a more limited progress in this case. Fig. 24 presents $h_{min}(\beta)$ for $\lambda = 0.25$ and a moderately small $Ca = 0.04$.The boundary-integral results for $N_\triangle = 15$K and 35K are in close agreement, but both differ considerably from the prediction of the $\tilde{\lambda} = 0$ asymptotic theory; for the same $Ca = 0.04$ and $\lambda = 1$, this theory was much more successful (cf. Fig. 16(a) and Fig. 24). At $\lambda = 0.25$, the primary reason for the discrepancy in the separation zone is presumably a vigorous pumping flow. At the initial stage of approach, however, the discrepancy is mostly due to neglect of other high-order terms in thin-film equations (it is known [22] that, even apart from pumping-flow effects, the leading-order asymptotic theory is limited to $\lambda \gg O(Ca^{1/2}|\ln Ca|)$). It was found too difficult to extend convergent boundary-integral results in Fig. 24 to much smaller Ca and validate the asymptotic theory, since the surface separation is already very small at $Ca = 0.04$, due to low thin-film resistance for $\lambda = 0.25$ (cf. Fig. 16(a) and Fig. 24). Until high-order asymptotic theories are implemented (with pumping included), convergent boundary-integral calculations can be the only source of reliable information for $\lambda \ll 1$ and $Ca \ll 1$. Note that the $\tilde{\lambda} \neq 0$ asymptotic version would not make sense at all for $\lambda \ll 1$.

7. Conclusions

We have developed a novel three-dimensional, multipole-accelerated boundary-integral algorithm to study gravity-induced and shear-induced motion of two drops in close contact at zero Reynolds number and very small capillary numbers Ca, when the drops are nearly spherical. Although $Ca \ll 1$ interactions may look like a specialized case, it is, in fact, the only case relevant to coalescence of drops with not too small viscosity ratio λ in a Stokes flow; with finite deformations ($Ca = O(1)$), such drops simply do not come close enough for van der Waals forces to become significant and initiate coalescence, at least for realistic values of the parameters. Numerically, the case $Ca \ll 1$ is far more difficult than the two-drop motion at moderate deformations, because of very tight stability limitations on the time step and the capillary number providing a singular perturbation; very high resolution is needed both in the small gap and in the outer region, as $Ca \to 0$. For $N_\triangle \sim 10^5$ triangular elements per drop, essential in this type of simulations to accurately trace surface clearance h_{min} to less than $0.001a_i$, our algorithm has, at least, an order-of-magnitude

gain over the standard boundary-integral method, making such long-time dynamical simulations feasible. Besides multipole acceleration, our method features a novel and relatively simple "dynamical projective mesh" technique, to adapt fixed topology triangulations to the gap. A versatile and general mesh restructuring algorithm has been recently developed and found suitable for drop interactions with large to moderately small deformations [24]. At $Ca \to 0$, on the other hand, we have found the present "dynamical projective mesh" technique to be very robust.

Our code has provided a new opportunity to obtain exact results for general two-drop relative motion in close contact at $Ca \ll 1$ and arbitrary λ, and determine the range of validity of asymptotic theories (based on axisymmetrical thin-film solutions in the gap matched with the outer solution for spherical drops). Both the dynamics of the surface clearance $h_{\min}$ and the separation angle β_{sep} have been studied. For $\lambda = 1$, the asymptotic theory slightly overestimates β_{sep} in gravity-induced motion, but underpredicts it in shear-induced motion. In the latter case, the error in the separation angle decreases from 0.085 rad to about 0.022 rad, as Ca is decreased from 0.04 to 0.005; this discrepancy is attributed to the pumping flow effect neglected in the asymptotic theory. For $h_{\min}$, the asymptotic theory [22,23] provides excellent accuracy at $Ca \leqslant 0.02$ in shear-induced motion, except for $\beta \approx \beta_{\text{sep}}$. The minimum clearance along a trajectory, $\min h_{\min}/a$, has a scaling $\mathrm{O}(Ca^{4/3})$, as $Ca \to 0$, while the separation angle β_{sep} approaches $\pi/2$ (corresponding to zero driving force in the asymptotic theory) extremely slowly, with an error of $\mathrm{O}(Ca^{1/3})$.

We also extended an efficient, absolutely stable thin-film algorithm [22] to high viscosity ratios λ and derived a new matching condition with the outer trajectory, to arrive at an asymptotic version suitable for $\lambda \gg 1$. For drops with $\lambda = 4$ and 10 in shear flow, this asymptotic theory was shown to be very accurate, compared to exact results, both for $h_{\min}$ and β_{sep} in the wide range of $Ca \ll 1$. An unresolved question, though, is whether this $\lambda \gg 1$ theory would be as successful for much higher λ, since the tangential motion may start to be affected by deformations at $\lambda \to \infty$.

In contrast, for $\lambda = 0.25$ and $Ca = 0.04$ in shear flow, we have found the asymptotic approach to be quite unsuccessful due to a much stronger pumping flow effect and neglect of other high-order terms in thin-film equations. An adequate, high-order asymptotic algorithm valid for $\lambda \ll 1$ in the wide range of $Ca \ll 1$ has yet to be developed; at present, convergent boundary-integral calculations, albeit difficult, can provide the only source of reliable information in this case.

It was recently found [24,25] that two deformable drops pressed together by an axisymmetrical compressional flow reach a steady state with non-zero gap thickness (due to the pumping flow pulling fluid into the gap and balancing the squeezing effect), instead of continuous film thinning predicted by the leading-order asymptotic theory for $Ca \ll 1$ based on the concept of the "driving force." One can also question if the approximation of local axial symmetry of the thin film is valid for non-axisymmetrical collisions. Despite striking qualitative difference between the exact calculations and leading-order thin-film theory predictions for head-on collisions, our entire analysis shows that it is safe to use the leading-order asymptotic theories (which neglect pumping flow effects and assume local axial symmetry) for generic, non-axisymmetrical collisions in the wide range of $Ca \ll 1$ and $\lambda \geqslant \mathrm{O}(1)$; typical times of such interactions are too short for the pumping flow to have a strong effect. This conclusion justifies, in particular, extensive coalescence efficiency calculations done by the asymptotic method [22,23] for $\lambda = \mathrm{O}(1)$. The applicability of the leading-order asymptotic theories to nearly head-on collisions, however, would require a separate study. The result may be non-trivial, since, in some range of parameters, only collisions close to head-on lead to coalescence.

Our algorithm can be generalized for the presence of an insoluble surfactant or temperature gradient. Besides, using the half-space Green function [37] instead of the free-space Green function, it is possible to extend our 3D techniques to close interaction of a deformable drop and a plane wall at $Ca \ll 1$ – the case where high, gap-adaptive triangulations would be also required. Potential applications include gravity-driven drop motion along an inclined wall, and a study of flow-induced steady states in addition to analytical ideas [25].

Appendix A. Lamb's series for a symmetric tensor field

Let $\boldsymbol{v}^k$ ($k = 1,2,3$) be three Stokes flows; $\boldsymbol{v}^k = (v_1^k, v_2^k, v_3^k)$ in Cartesian coordinates, and $v_j^k = v_k^j$. Let $\boldsymbol{v}^k(\boldsymbol{r})$ be expanded for $r > d$ as Lamb's singular series

$$\boldsymbol{v}^k(\boldsymbol{r}) = \sum_{v=1}^{\infty}\left[\nabla\times\left(\boldsymbol{r}\tilde{\chi}^k_{-(v+1)}\right) + \nabla\tilde{\Phi}^k_{-(v+1)} - \frac{(v-2)r^2\nabla\tilde{p}^k_{-(v+1)}}{2v(2v-1)} + \frac{(v+1)\tilde{p}^k_{-(v+1)}\boldsymbol{r}}{v(2v-1)}\right] + \nabla\tilde{\Phi}^k_{-1}, \tag{A.1}$$

where

$$\begin{aligned}
&\tilde{p}^k_{-(v+1)}(\boldsymbol{r}) = \sum_{\mu=-v}^{v} A^k_{-(v+1),\mu}\left(\frac{d}{r}\right)^{v+1} Y_{v,\mu}(\boldsymbol{r}), \quad \tilde{\Phi}^k_{-(v+1)}(\boldsymbol{r}) = \sum_{\mu=-v}^{v} B^k_{-(v+1),\mu}\left(\frac{d}{r}\right)^{v+1} Y_{v,\mu}(\boldsymbol{r}),\\
&\tilde{\chi}^k_{-(v+1)}(\boldsymbol{r}) = \sum_{\mu=-v}^{v} C^k_{-(v+1),\mu}\left(\frac{d}{r}\right)^{v+1} Y_{v,\mu}(\boldsymbol{r}), \quad A^k_{-(v+1),-\mu} = (-1)^{\mu}\overline{A}^k_{-(v+1),\mu}, \ldots
\end{aligned} \tag{A.2}$$

and $Y_{v,\mu}(\boldsymbol{r})$ is the standard normalized spherical harmonic

$$\begin{aligned}
&Y_{v,\mu}(\boldsymbol{r}) = \left[\frac{(2v+1)(v-\mu)!}{4\pi(v+\mu)!}\right]^{1/2} P_v^{\mu}(\cos\theta)\,\mathrm{e}^{\mathrm{i}\mu\varphi} \quad (\mu \geqslant 0),\\
&Y_{v,\mu}(\boldsymbol{r}) = (-1)^{\mu}\overline{Y}_{v,-\mu}(\boldsymbol{r}) \quad (\mu < 0),
\end{aligned} \tag{A.3}$$

for a vector $\boldsymbol{r} = (r\sin\theta\cos\varphi, r\sin\theta\sin\varphi, \cos\theta)$, P_v^{μ} is the associated Legendre function (in the notations [38]); the overbar denotes complex conjugation. The associated vector of pressures $\boldsymbol{p} = (\tilde{p}^1, \tilde{p}^2, \tilde{p}^3)$ is [39]

$$\boldsymbol{p} = \sum_{v=1}^{\infty}\boldsymbol{p}_{-(v+1)}, \quad \boldsymbol{p}_{-(v+1)} = \left(\tilde{p}^1_{-(v+1)}, \tilde{p}^2_{-(v+1)}, \tilde{p}^3_{-(v+1)}\right). \tag{A.4}$$

Special relations exist between the coefficients in (A.2), due to the symmetry of tensor v_j^k. First, $\nabla^2 v_j^k = D_j p^k$ (where D_j is the partial derivative along the jth Cartesian coordinate) and $v_j^k = v_k^j$ immediately yield $\nabla\times\boldsymbol{p} = 0$. Note that $\nabla\times\boldsymbol{p}_{-(v+1)}$ is a combination of solid harmonics of order $-(v+2)$; due to orthogonality of $Y_{n,m}$, one obtains

$$\nabla\times\boldsymbol{p}_{-(v+1)} = 0, \quad v = 1,2,\ldots \tag{A.5}$$

Next, we use the general relation [39]

$$(\nabla\times\boldsymbol{v}^k)\cdot\boldsymbol{r} = \sum_{v=1}^{\infty} v(v+1)\tilde{\chi}^k_{-(v+1)}. \tag{A.6}$$

Differentiating the LHS of (A.6), using the continuity equation and the symmetry $v_j^k = v_k^k$ yields

$$D_k\left[(\nabla\times\boldsymbol{v}^k)\cdot\boldsymbol{r}\right] = D_k\left[\varepsilon_{\alpha\beta\gamma}r_\gamma D_\alpha v_\beta^k\right] = \varepsilon_{\alpha\beta k}D_\alpha v_\beta^k = 0, \tag{A.7}$$

where $\varepsilon_{\alpha\beta\gamma}$ is the Levy–Chivita tensor. Again, $D_k\tilde{\chi}^k_{-(v+1)}$ is a combination of solid harmonics of order $-(v+2)$; from (A.6) and (A.7) and orthogonality of $Y_{n,m}$, we derive

$$\nabla\cdot\boldsymbol{\chi}_{-(v+1)} = 0, \quad \boldsymbol{\chi}_{-(v+1)} = \left(\tilde{\chi}^1_{-(v+1)}, \tilde{\chi}^2_{-(v+1)}, \tilde{\chi}^3_{-(v+1)}\right), \quad v = 1,2,\ldots \tag{A.8}$$

Using the well-known relations

$$(D_1 \pm \mathrm{i}D_2)\frac{Y_{n,m}(\boldsymbol{r})}{r^{n+1}} = \mp\left[\frac{(2n+1)(n\pm m+1)(n\pm m+2)}{2n+3}\right]^{1/2}\frac{Y_{n+1,m\pm1}(\boldsymbol{r})}{r^{n+2}},$$
$$D_3\frac{Y_{n,m}(\boldsymbol{r})}{r^{n+1}} = -\left[\frac{(2n+1)(n-m+1)(n+m+1)}{2n+3}\right]^{1/2}\frac{Y_{n+1,m}(\boldsymbol{r})}{r^{n+2}}, \tag{A.9}$$

one can obtain from (A.2), (A.5) and (A.8), after some algebra

$$A^1_{-(v+1),\mu} = fA^3_{-(v+1),\mu-1} - gA^3_{-(v+1),\mu+1}, \quad A^2_{-(v+1),\mu} = -i\left[fA^3_{-(v+1),\mu-1} + gA^3_{-(v+1),\mu+1}\right], \tag{A.10}$$

and

$$C^3_{-(v+1),\mu} = g\left[C^1_{-(v+1),\mu+1} + iC^2_{-(v+1),\mu+1}\right] - f\left[C^1_{-(v+1),\mu-1} - iC^2_{-(v+1),\mu-1}\right], \tag{A.11}$$

where $f = \frac{1}{2}[(v+\mu)/(v-\mu+1)]^{1/2}$ and $g = \frac{1}{2}[(v-\mu)/(v+\mu+1)]^{1/2}$.Using (A.10) and (A.11) allows one to considerably optimize generation of the expansions (3.8) compared to the threefold repetition of the algorithm of [10] (Section 3.2 therein) for $k = 1,2,3$.Namely, expansions (3.8) are first generated for each individual node $\boldsymbol{x}_j \in \mathscr{B}_\gamma$ in "intrinsic" coordinates (the z-axis being along $\boldsymbol{x}_j - \boldsymbol{x}^o_\gamma$), with only coefficients $A^3_{-(v+1),\mu}$, $B^k_{-(v+1),\mu}$ $(k = 1,2,3)$ and $C^k_{-(v+1),\mu}$ $(k = 1,2)$ calculated in (A.2).According to the algebra [10], this O(max v)-intensive but cumbersome step is greatly simplified by using intrinsic coordinates for the vectors in the LHS of (3.8); only $|\mu| \leqslant 2$ is essential in these coordinates.The remaining coefficients are taken from (A.10) and (A.11), and the basis transformation is then made, to represent the original coordinates $\tilde{p}^3_{-(v+1),\mu}$, $\tilde{\Phi}^k_{-(v+1),\mu}$ $(k = 1,2,3)$, and $\tilde{\chi}^k_{-(v+1),\mu}$ $(k = 1,2)$ in the form (A.2), with harmonics $Y_{v,\mu}$ still written in the intrinsic coordinates.The next, O(max v^2)-intensive step, is to subject $Y_{v,\mu}$ to rotational transformations into the original coordinate system, with the corresponding recalculation of $A^3_{-(v+1),m}$, $B^k_{-(v+1),m}$ $(k = 1,2,3)$ and $C^k_{-(v+1),m}$ $(k = 1,2)$, and accumulate these coefficients for all $\boldsymbol{x}_j \in \mathscr{B}_\gamma$. Finally, relations (A.10) and (A.11) are used to restore the remaining cumulative coefficients $A^k_{-(v+1),m}$ $(k = 1,2)$ and $C^3_{-(v+1),m}$ in the original coordinates. For practically used $v \leqslant 20$–30, this logic generates the expansions (3.8) more than two times faster compared to the threefold repetition of the algorithm of [10] for $k = 1,2,3$.

Now, let $\boldsymbol{v}^k(\boldsymbol{r}) = (v^k_1, v^k_2, v^k_3)$, with $k = 1,2,3$, be a symmetric Stokes tensor, expanded for $r < d$ as Lamb's regular series

$$\boldsymbol{v}^k(\boldsymbol{r}) = \sum_{n=1}^{\infty}\left[\nabla\times(\boldsymbol{r}\chi^k_n) + \nabla\Phi^k_n + \frac{(n+3)r^2\nabla p^k_n}{2(n+1)(2n+3)} - \frac{np^k_n\boldsymbol{r}}{(n+1)(2n+3)}\right], \tag{A.12}$$

where

$$p^k_n(\boldsymbol{r}) = \sum_{m=-n}^{n} A^k_{n,m}\left(\frac{r}{d}\right)^n Y_{n,m}(\boldsymbol{r}), \quad \Phi^k_n(\boldsymbol{r}) = \sum_{m=-n}^{n} B^k_{n,m}\left(\frac{r}{d}\right)^n Y_{n,m}(\boldsymbol{r}),$$
$$\chi^k_n(\boldsymbol{r}) = \sum_{m=-n}^{n} C^k_{n,m}\left(\frac{r}{d}\right)^n Y_{n,m}(\boldsymbol{r}), \quad A^k_{n,-m} = (-1)^m\overline{A}^k_{n,m}, \ldots \tag{A.13}$$

Similar to (A.5) and (A.7), we have

$$\nabla\times\boldsymbol{p}_n = 0, \quad \nabla\cdot\boldsymbol{\chi}_n = 0, \tag{A.14}$$

where $\boldsymbol{p}_n = (p^1_n, p^2_n, p^3_n)$ and $\boldsymbol{\chi}_n = (\chi^1_n, \chi^2_n, \chi^3_n)$. By the recurrent formulae for $(D_1 \pm \mathrm{i}D_2)r^n Y_{n,m}(\boldsymbol{r})$ and $D_3 r^n Y_{n,m}(\boldsymbol{r})$ similar to (A.9), the constraints (A.14) can be shown to give

$$
\begin{aligned}
&(n-m+1)^{1/2}A^3_{n,m-1} + (n+m)^{1/2}\left[A^1_{n,m} + iA^2_{n,m}\right] = 0,\\
&(n+m+1)^{1/2}A^3_{n,m+1} - (n-m)^{1/2}\left[A^1_{n,m} - iA^2_{n,m}\right] = 0,\\
&-[(n-m)(n-m+1)]^{1/2}\left[C^1_{n,m-1} - \mathrm{i}C^2_{n,m-1}\right] + 2[(n-m)(n+m)]^{1/2}C^3_{n,m}\\
&\quad + [(n+m)(n+m+1)]^{1/2}\left[C^1_{n,m+1} + \mathrm{i}C^2_{n,m+1}\right] = 0.
\end{aligned}
\tag{A.15}
$$

Unlike in (A.10) and (A.11), Eq. (A.15) can be resolved for $(A^1_{n,m}, A^2_{n,m})$ and $C^3_{n,m}$ only at $|m| < n$. Using (A.15) together with (A.10) and (A.11) allows us to optimize rotation-based reexpansions from (3.8) to regular forms (3.9) in the following manner. The coordinates $A^3_{-(\nu+1),\mu}$, $B^k_{-(\nu+1),\mu}$ $(k = 1,2,3)$, $C^k_{-(\nu+1),\mu}$ $(k = 1,2)$ of vectors $\boldsymbol{A}_{-(\nu+1),\mu}$, $\boldsymbol{B}_{-(\nu+1),\mu}$ and $\boldsymbol{C}_{-(\nu+1),\mu}$ are transformed to a new "axial" basis (the z-axis being along the reexpansion vector $\boldsymbol{x}^o_\delta - \boldsymbol{x}^o_\gamma$, see [10]), with harmonics $Y_{\nu,\mu}$ still written in the original coordinates. Then, $Y_{\nu,\mu}$ are subject to rotational transformation into the axial coordinate system, with corresponding recalculation of $A^3_{-(\nu+1),m}$, $B^k_{-(\nu+1),m}$ $(k = 1,2,3)$ and $C^k_{-(\nu+1),m}$ $(k = 1,2)$; the remaining coefficients $A^1_{-(\nu+1),m}$, $A^2_{-(\nu+1),m}$ and $C^3_{-(\nu+1),m}$ in the axial coordinates are taken from (A.10) and (A.11). Next, reexpansions of (3.8) to regular forms (3.9) are made in the axial coordinates for all $k = 1,2,3$, vectors $\boldsymbol{A}_{n,m}$, $\boldsymbol{B}_{n,m}$, $\boldsymbol{C}_{n,m}$ are recalculated in the original basis, and the coordinates $A^3_{n,m}$, $B^k_{n,m}$ $(k = 1,2,3)$, $C^k_{n,m}$ $(k = 1,2)$ are then subject to rotational transformation of spherical harmonics into the original coordinate system; diagonal elements $A^1_{n,n}$, $C^3_{n,n}$ are also calculated after rotation at a small additional cost. Finally, the remaining coefficients $A^1_{n,m}$, $A^2_{n,m}$, $C^3_{n,m}$ $(0 \leqslant m < n)$, and $A^2_{n,n}$ in the original coordinates are determined by (A.15). This procedure was found to be about 1.5 times faster compared to the threefold repetition of reexpansion algorithm [10] for $k = 1,2,3$.

Appendix B. Economical truncation bounds

The coefficients a_k in the expansion

$$
\sum_{\boldsymbol{x}_j \in \mathscr{B}_\gamma} \boldsymbol{G}(\boldsymbol{x}_j - \boldsymbol{y}) \cdot \boldsymbol{n}(\boldsymbol{x}_j)\Delta S_j = \sum_{k=0}^{\infty} a_k \left(\frac{d^o_\gamma}{R_\gamma}\right)^{k+1}, \quad R_\gamma > d^o_\gamma
\tag{B.1}
$$

are estimated like in [10] (Eqs. (3.83) and (3.84) therein), now through

$$
C_\gamma = \frac{1}{4\pi d^o_\gamma}\left\| \sum_{\boldsymbol{x}_j \in \mathscr{B}_\gamma} \boldsymbol{n}(\boldsymbol{x}_j)\Delta S_j \right\|.
\tag{B.2}
$$

Let

$$
f_{\max}(\delta,\beta) = \max_{\boldsymbol{y} \in \mathscr{B}_\delta} |\Theta(\boldsymbol{y},\beta) f(\boldsymbol{x}^*)|,
\tag{B.3}
$$

be the majorant on the coefficient $\Theta f(\boldsymbol{x}^*)$ in (3.2) for a patch $\mathscr{B}_\delta$ interacting with drop S_β. Accordingly, the tolerance ε_1 in the relation (3.87) of [10] allowing calculation of the truncation bounds associated with (3.7) is modified to

$$
\varepsilon_1 = \left[\sum_{\beta=1}^{2} f_{\max}(\delta,\beta) \sum_{\mathscr{B}_\gamma \subset S_\beta} R^{-4}_{\delta\gamma}\right]^{-1} e_{\mathrm{nf}} R^{-4}_{\delta\gamma}\varepsilon, \quad R_{\delta\gamma} = \left\|\boldsymbol{x}^o_\gamma - \boldsymbol{x}^o_\delta\right\|.
\tag{B.4}
$$

Here, the summation is over all patches $\mathscr{B}_\gamma$ on both drops excluding $\mathscr{B}_\delta$. The new form (B.4) guarantees that the cumulative truncation error of multipole calculations of the second sum (3.2) from all blocks $\mathscr{B}_\gamma \neq \mathscr{B}_\delta$ is less than $e_{\rm nf}\varepsilon$ (where $e_{\rm nf} = {\rm O}(1)$ is a chosen numerical factor).

Similar modifications are made to the scheme of [10] to calculate the economical truncation bounds associated with the subtraction tensor expansion (3.8). The coefficients $\tilde{a}_n^k$ in the expansion

$$\frac{1}{2}\sum_{n=1}^{\infty}\tilde{a}_n^k\left(\frac{d_\gamma^o}{R_\gamma}\right)^{n+1}, \quad R_\gamma > d_\gamma^o, \tag{B.5}$$

for the RHS of (3.8) are estimated like in (3.91) of [10], now through

$$\tilde{C}_\gamma = \frac{3}{2\pi(d_\gamma^o)^2}\left\|\sum_{\boldsymbol{x}_j\in\mathscr{B}_\gamma}\boldsymbol{n}(\boldsymbol{x}_j)\Delta S_j\right\|. \tag{B.6}$$

Let

$$Q_{\max}(\delta,\beta) = \max_{\boldsymbol{y}\in\mathscr{B}_\delta}\|\Theta(\boldsymbol{y},\beta)\boldsymbol{Q}(\boldsymbol{x}^*)\| \tag{B.7}$$

be the majorant on the coefficient $\Theta\boldsymbol{Q}(\boldsymbol{x}^*)$ in (3.3) for a patch $\mathscr{B}_\delta$ interacting with drop S_β. The tolerance ε_1 in Eq. (3.87) of [10] to calculate the truncation bounds for the subtraction tensor expansions (3.8) and re-expansions (3.9) now reads

$$\varepsilon_1 = \frac{2}{|\lambda-1|}\left[\sum_{\beta=1}^{2}Q_{\max}(\delta,\beta)\sum_{\mathscr{B}_\gamma\subset S_\beta}R_{\delta\gamma}^{-4}\right]^{-1}\tilde{e}_{\rm nf}R_{\delta\gamma}^{-4}\varepsilon, \tag{B.8}$$

where $\tilde{e}_{\rm nf} = {\rm O}(1)$ is another numerical factor, and $\gamma = \delta$ is excluded, again, from the summation. In other respects, the calculation of the truncation bounds proceeds like in (3.86)–(3.91) of [10]. Parameters $e_{\rm nf} = 1$ and $\tilde{e}_{\rm nf} = 3$ were determined experimentally in the present problem to balance, approximately, the truncation errors for the inhomogeneous $\boldsymbol{F}(\boldsymbol{y})$ and double-layer terms. With $e_{\rm nf}$ and $\tilde{e}_{\rm nf}$ fixed, our truncation scheme depends on a single precision parameter ε.

Appendix C. Rescaling of thin-film equations at $\beta \approx \pi/2$

Consider, for simplicity, the case of gravity–induced motion. Let $\tilde{t}_o$ be the value of the non-dimensional time (4.10) $\tilde{t}$, corresponding to $\beta = \pi/2$. Dynamics (4.3) of the β-angle yields

$$\beta(\tilde{t}) = 2\arctan\left\{\exp\left[\zeta Ca^{1/2}(\tilde{t}-\tilde{t}_0)\right]\right\} \approx \frac{\pi}{2} + \zeta Ca^{1/2}(\tilde{t}-\tilde{t}_o), \tag{C.1}$$

where

$$\zeta = \frac{2}{3}\frac{\lambda}{(k+1)}\left[\frac{2\pi}{(1-k^2)}\frac{(\lambda+\frac{2}{3})}{(\lambda+1)}\right]^{1/2}T, \tag{C.2}$$

and linearization in (C.1) was made for $\beta \approx \pi/2$. Upon substitution of (C.1) into (4.18), further simplification is made: $\cos\beta \approx -\zeta Ca^{1/2}(\tilde{t}-\tilde{t}_o)$. In the new, rescaled variables

$$\hat{r} = \frac{\tilde{r}}{\omega^{1/3}Ca^{1/6}}, \quad \hat{h} = \frac{\tilde{h}}{\omega^{2/3}Ca^{1/3}}, \quad \hat{t} = \omega^{1/3}Ca^{1/6}(\tilde{t}-\tilde{t}_o), \quad \hat{p} = \tilde{p}, \quad \hat{u} = \frac{\tilde{u}}{\omega^{2/3}Ca^{1/3}}, \quad \hat{f} = \frac{\tilde{f}}{\omega^{1/3}Ca^{1/6}}, \tag{C.3}$$

where $\omega = \alpha\zeta$, and α is defined in (4.18), the thin-film equations (4.11)–(4.14) with $\tilde{\lambda} = 0$ remain invariant, while the force balance (4.15) becomes

$$\int_0^\infty \hat{p}\hat{r}\,\mathrm{d}\hat{r} = -\hat{t}. \tag{C.4}$$

Thus, in the rescaled variables (C.3), all thin-film equations at $\beta \approx \pi/2$ have a *universal* form not containing any parameters, in particular, the capillary number. The separation time $\hat{t}_{\mathrm{sep}}$ must be therefore O(1), which corresponds to $\beta_{\mathrm{sep}} = \frac{\pi}{2} + \mathrm{O}(Ca^{1/3})$, using (C.1) and (C.3).

The same universality arguments are used to find scaling for the local minimum, $\min h_{\mathrm{min}}$, of the gap at the separation point. Namely, $\hat{h}$ must be O(1) at separation, which yields, using (4.10) and (C.3)

$$\min h_{\mathrm{min}}/a_2 \sim Ca^{4/3}, \quad Ca \to 0. \tag{C.5}$$

When there are more than one local minima of h_{min}, the numerical examples of Section 6.2 show that the scaling (C.4) still holds for the entire near-contact motion between the minima.

References

[1] M. Loewenberg, E.J. Hinch, Collision of two deformable drops in shear flow, J. Fluid Mech. 338 (1997) 299–315.
[2] M. Manga, H.A. Stone, Bouyancy-driven interactions between two deformable viscous drops, J. Fluid Mech. 256 (1993) 647–683.
[3] M. Manga, H.A. Stone, Collective hydrodynamics of deformable drops and bubbles in dilute low Reynolds number suspensions, J. Fluid Mech. 300 (1995) 231–263.
[4] A.Z. Zinchenko, M.A. Rother, R.H. Davis, Cusping capture and breakup of interacting drops by a curvatureless boundary-integral algorithm, J. Fluid Mech. 391 (1999) 249–292.
[5] V. Cristini, J. Bławzdziewicz, M. Loewenberg, Drop breakup in three-dimensional viscous flows, Phys. Fluids 10 (1998) 1781–1783.
[6] M. Loewenberg, E.J. Hinch, Numerical simulation of a concentrated emulsion in shear flow, J. Fluid Mech. 321 (1996) 395–419.
[7] M. Loewenberg, Numerical simulation of concentrated emulsion flows, J. Fluid Eng. 120 (1998) 824–832.
[8] A.Z. Zinchenko, R.H. Davis, Shear flow of highly concentrated emulsions of deformable drops by numerical simulations, J. Fluid Mech. 455 (2002) 21–62.
[9] D.L. Koch, E.S.G. Shaqfeh, The instability of dispersion of sedimenting spheroids, J. Fluid Mech. 209 (1989) 521–542.
[10] A.Z. Zinchenko, R.H. Davis, An efficient algorithm for hydrodynamical interaction of many deformable drops, J. Comput. Phys. 157 (2000) 539–587.
[11] A.Z. Zinchenko, R.H. Davis, Large-scale simulations of concentrated emulsion flows, Phil. Trans. R. Soc. Lond. A 361 (2003) 813–845.
[12] J.M. Rallison, A. Acrivos, A numerical study of the deformation and burst of a viscous drop in an extensional flow, J. Fluid Mech. 89 (1978) 191–200.
[13] B.E. Burkhart, P.V. Gopalkrishnan, S.D. Hudson, A.M. Jamieson, M.A. Rother, R.H. Davis, Droplet growth by coalescence in binary mixtures, Phys. Rev. Lett. 87 (2001) 098304.
[14] S.D. Hudson, A.M. Jamieson, B. Burkhart, The effect of surfactant on the efficiency of shear-induced drop coalescence, J. Colloid Interface Sci. 265 (2003) 409–421.
[15] J.W. Ha, Y. Yoon, L.G. Leal, The effect of compatibilizer on the coalescence of two drops in flow, Phys. Fluids 15 (2003) 849.
[16] S.G. Yiantsios, R.H. Davis, On the buoyancy-driven motion of a drop towards a rigid surface or a deformable interface, J. Fluid Mech. 217 (1990) 547–573.
[17] S.G. Yiantsios, R.H. Davis, Close approach and deformation of two viscous drops due to gravity and van der Waals forces, J. Colloid Interface Sci. 144 (1991) 412–433.
[18] A.Z. Zinchenko, Calculation of the effectiveness of gravitational coagulation of drops with allowance for internal circulation, J. Appl. Math. Mech. 46 (1983) 58–65.
[19] A.Z. Zinchenko, Calculation of close interaction between drops with internal circulation and slip effect taken into account, J. Appl. Math. Mech. 45 (1982) 564–567.
[20] R.H. Davis, J.A. Schonberg, J.M. Rallison, The lubrication force between two viscous drops, Phys. Fluids A 1 (1989) 77–81.
[21] I. Bazhlekov, A. Chesters, F. van de Vosse, The effect of the dispersed to continuous-phase viscosity ratio on film drainage between interacting drops, Int. J. Mult. Flow 26 (2000) 445.

[22] M.A. Rother, A.Z. Zinchenko, R.H. Davis, Buoyancy-driven coalescence of slightly deformable drops, J. Fluid Mech. 346 (1997) 117–148.
[23] M.A. Rother, R.H. Davis, The effect of slight deformation on droplet coalescence in linear flows, Phys. Fluids 13 (2001) 1178–1190.
[24] V. Cristini, J. Bławzdziewicz, M. Loewenberg, An adaptive mesh algorithm for evolving surfaces: simulations of drop breakup and coalescence, J. Comput. Phys. 168 (2001) 445–463.
[25] M.B. Nemer, X. Chen, D.H. Papadopoulos, J. Bławzdziewicz, M. Loewenberg, Hindered and enhanced coalescence of drops in Stokes flow, Phys. Rev. Lett. 92 (2004) 114501.
[26] A.S. Sangani, G. Mo, An O(N) algorithm for Stokes and Laplace interactions of particles, Phys. Fluids 8 (1996) 1990–2010.
[27] S. Kim, S. Karilla, Microhydrodynamics: Principles and Selected Applications, Butterworth–Heinemann, Boston, MA, 1991.
[28] C. Pozrikidis, Boundary Integral and Singularity Methods for Linearized Viscous Flow, Cambridge University Press, Cambridge, 1992.
[29] A.Z. Zinchenko, M.A. Rother, R.H. Davis, A novel-boundary integral algorithm for viscous interaction of deformable drops, Phys. Fluids 9 (1997) 1493–1511.
[30] J.M. Rallison, A numerical study of the deformation and burst of a viscous drop in general shear flows, J. Fluid Mech. 109 (1981) 465–482.
[31] M.E. Staben, A.Z. Zinchenko, R.H. Davis, Motion of a particle between two parallel plane walls in low-Reynolds-number Poiseuille flow, Phys. Fluids 15 (2003) 1711–1733.
[32] L.D. Reed, F.A. Morrison, The slow motion of two touching fluid spheres along their line of centres, Int. J. Multiphase Flow 1 (1974) 573–583.
[33] A.Z. Zinchenko, The slow asymmetrical motion of two drops in a viscous medium, J. Appl. Math. Mech. 44 (1981) 30–37.
[34] H. Wang, A.Z. Zinchenko, R.H. Davis, The collision rate of small drops in linear flow fields, J. Fluid Mech. 265 (1994) 161–188.
[35] A.Z. Zinchenko, Hydrodynamic interaction of two identical liquid spheres in linear flow field, J. Appl. Math. Mech. 47 (1984) 37–43.
[36] A. Gopinath, D.L. Koch, Collision and rebound of small droplets in incompressible continuum gas, J. Fluid Mech. 454 (2002) 145–201.
[37] J.R. Blake, A note on the image system for a Stokeslet in a no-slip boundary, Proc. Cambridge Philos. Soc. 70 (1971) 303.
[38] G.A. Korn, T.M. Korn, Mathematical Handbook for Scientists and Engineers, McGraw-Hill, New York, 1968.
[39] J. Happel, H. Brenner, Low Reynolds Number Hydrodynamics, Nijhoff, Dordrecht, 1973.